Nano-engineering of Strong Field Processes in Solids

Kazi Shudipto Amin

Thesis submitted to the
Faculty of Graduate and Postdoctoral Studies
in partial fulfillment of the requirements for the degree of
MSc in Physics

Supervised by Thomas Brabec

Ottawa Carleton Institute of Physics
Department of Physics
University of Ottawa
Ottawa, Canada

Abstract

We investigate ionization and high harmonic generation (HHG) from the interaction of a mid infra-red laser pulse with a solid state system confined to nano-dimensions. The theory of strong field processes in solids is developed for confined quantum systems in general. Here it is applied to two-dimensional quantum wires with a driving field linearly polarised along the axis of the wires. Our findings indicate that that we are able to control the ionization and high-harmonic output by altering the width of the wire. Control of ionization leads to an increased damage threshold which has important implications for nano-engineering and realizing all solid state coherent XUV sources.

Acknowledgements

I would like to thank Thomas Brabec for giving me the opportunity to work on this project and for supporting me in the last two years. I am grateful to Chris McDonald for helping me understand the research, giving frequent suggestions and making sure I was on track. Thanks also to Charles Varin for the warm welcome and setting me up with Primus; to Graeme Bart and Rhys Emms for pizza and video game nights; to Nakib H. Protik for all his useful advice, inside and outside of academics, that made the ride a lot smoother.

I am very grateful to my significant other, Ishruna Muniyat (Riniki), for being patient and struggling to find a way to bridge this long distance gap. My parents get special thanks, for allowing me to dream and trying their best to get me closer to fulfilling them.

Contents

Introduction

The invention of the laser nearly six decades ago revolutionized the study of light-matter interaction, leading to the discovery of many new phenomena. One such phenomenon is harmonic generation, where multiple pump laser photons are parametrically converted into a single photon of higher energy, with a frequency that is an integer multiple, or 'harmonic' of the driving laser frequency [1]. This phenomenon is fundamental to the field of non-linear optics and was initially studied in the perturbative regime. However, with the developments in laser technology allowing for more intense pulses, the study of light-matter interaction was extended to the non-perturbative realm [2]. One of the most prominent outcomes of such interactions is **high harmonic generation** (HHG): the generation of coherent harmonics with frequencies many times the fundamental laser frequency [2–4]. This process is able to yield ultrafast pulses of unprecedented intensities on an attosecond (10^{-18}s) time-scale, which was previously unattainable [5]. This motivated the advent of attosecond science [4–6] and helped develop new ultrafast imaging methods such as molecular spectroscopy [7–10] and tomography [11, 12].

High harmonic generation in atoms

High harmonic generation was first observed in 1977 from the interaction of intense CO_2 laser pulses with plasma [13]. Since then HHG has been extensively studied in atomic and molecular gases [14–16]. As a result, the theory for HHG in these systems is well developed and widely accepted within the strong-field community [2–4]. Here we present a physical picture of the process using the **three-step model** for atomic HHG [2, 17].

In the following discussion, we neglect the magnetic component of the applied laser pulse and consider only the potential due to the electric field. Furthermore, since the applied pulse has a wavelength orders of magnitude larger than the atomic radius, we neglect the space dependence of the applied electric field; this is known as the dipole approximation [18]. Figure 1 qualitatively illustrates the three-step model under these assumptions. The electron (blue circle) is in a bound state in an atomic potential (black curve). The electric potential (red dashed line) skews the total potential, allowing the electron to tunnel ionise across the reduced potential barrier (step 1). Once ionised, the effect of the atomic potential is negligible due to the high intensity of the laser pulse, and the electron is accelerated solely by the temporally oscillating electric field (step 2). In the final step, the electron collides with the ion with a higher energy, and emits a harmonic photon upon recombination [2, 3].

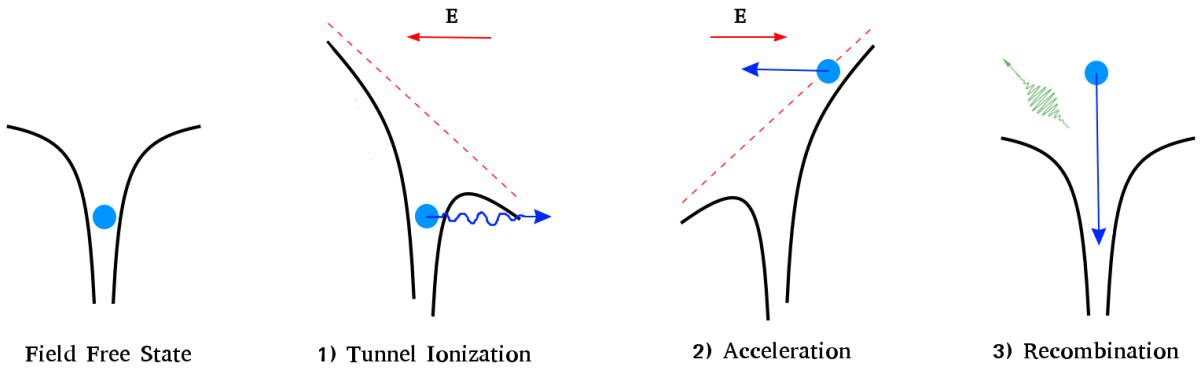

Figure 1: The three step model for HHG in atoms. The red dashed line is the electric potential, and the red arrow shows the direction of **E**, the electric field.

High harmonic generation in solids

While HHG was been extensively studied in atomic and molecular systems, very little attention has been paid to solid state systems. Recently, HHG was observed in 2011 for a ZnO crystal structure illuminated by a mid-infra red laser pulse of wavelength 3.25μm [19]. Since then, further experimental work involving bulk semiconductor crystals in the THz range [20, 21] and mid-IR [22, 23] ranges have been investigated. Furthermore, HHG has also been observed in dielectrics [24]. In tandem with the experimental work, there has been a growing compliment of theoretical work in recent years [25–30]. Here we present a qualitative picture for HHG in bulk solids. In the next chapter we will present the mathematical theory in detail.

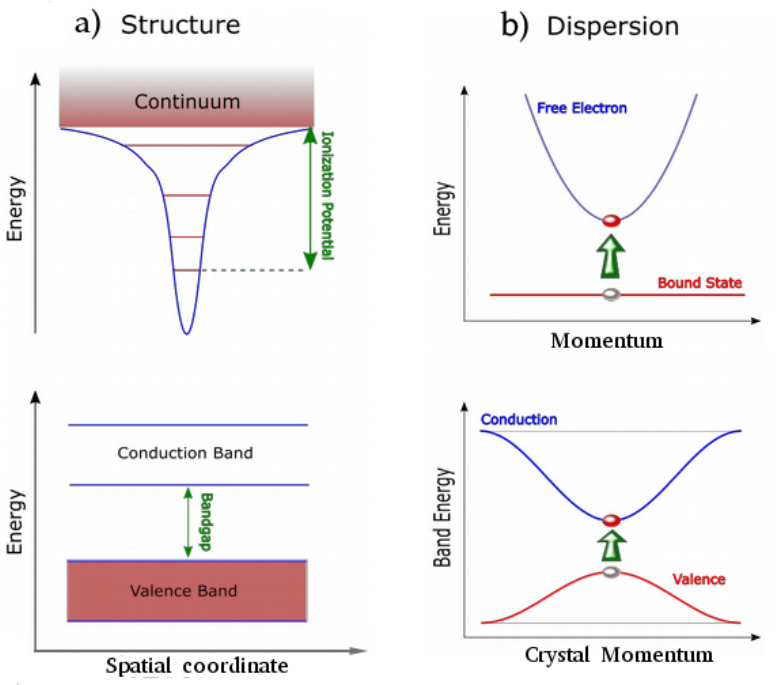

Figure 2: a) Comparison of atomic orbitals with solid band structure. b) Dispersion relations for electron in atoms and solids compared.[2]

For a better understanding of the mechanism behind HHG in solids, it is helpful to compare and contrast atoms with solids. In Fig.(2) we compare the band structure of solids with atomic energy levels (Fig. 2a) and the dispersion relationship of an electron in atoms with that of solids (Fig. 2b). In atomic HHG, an electron in an atomic orbital tunnel ionizes across an ionization potential into the continuum, where it obeys a parabolic dispersion relationship given by its energy as a function of momentum, **k**. Similarly for HHG in solids, an electron in the valence band ionizes across a band gap into the conduction band, where the dispersion relationship is given by the energy as a function of the **crystal momentum**, or wave vector, **k** [31, 32].

One of the key differences between the atomic case and the case in solids is that in atoms the positive ion is much heavier than the electron and has relatively little motion in the driving field. In solids, however, the hole left by the electron in the valence band has a comparable mass, so its motion also needs to be taken into account. Another difference is that in solids we have two sources of HHG, **interband** current and **intraband** current. Intraband current arises due to motion of an electron or hole within a band. In contrast, the interband current occurs due to the transition of electrons between bands and is calculated as the rate of change of the total polarization. At first, the intraband mechanism was thought to be the dominant mechanism, which it usually is for low order harmonics. However, recently it has been theoretically shown that the interband current dominates the harmonic spectrum for harmonic orders with energies above the minimum bandgap of the solid [28, 29]. This has been confirmed by experimental observation in 2015 [22].

Interband mechanism

It has been shown that interband harmonics are driven by a process similar to the three-step model of atomic HHG [28, 29]; this process if depicted in Fig.(3). An an electron from the valence band tunnel ionises to the conduction band (step 1); it then moves under the influence of the driving field (step 2), obeying the dispersion relation for the conduction band. Finally, it recombines with the hole at some crystal momentum **k** and emits a harmonic photon with energy equal to the band gap at **k**. The similarity of this process to that of the three-step model for HHG in atoms provides a connection between attosecond science and solid state physics — two previously disjoint fields. This also implies that it may be possible to extend the tools developed for attosecond science to solid state systems. A quantitative treatment

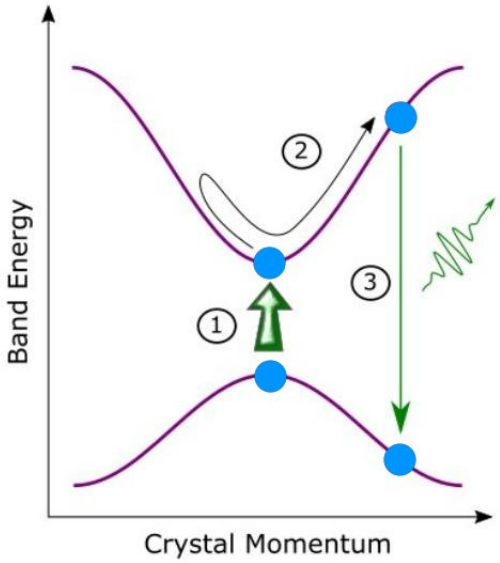

Figure 3: Three step model for interband mechanism in solids.[2]

[2]Reproduced with permission of C. McDonald

of the interband mechanism is provided at the end of Chapter 1.

Confined quantum systems

While high harmonics have been studied in bulk crystals, they have yet to be investigated in confined quantum systems. Through confinement these structures effectively become low dimensional systems having zero (quantum dots), one (quantum wire) or two (quantum wells) dimensions [33]. These structures have many applications in quantum computing, biotechnology and photovoltaic devices [34,35]. Reducing dimensions changes the density of states, affecting fundamental processes such as ionization, quantum diffusion and evolution in a strong field. As a result, lower-dimensional quantum systems can be used to nano-engineer strong field processes in solids. Here we will confine our analysis to a quantum wire and leave the other low dimensional systems for future research.

A **quantum wire** or nanowire is an electrically conducting wire with a narrow enough width that the electrons in the wire experience quantum confinement in the transverse directions, while along the axis of the wire their motion is unimpeded. The emergence of quantum effects due to spatial confinement can drastically change the optical properties of the material it is made of, thus nanowires hold great potential in optoelectronics such as nanowire lasers [36]. The main goal of this thesis is to provide a theoretical framework for strong field processes in confined systems that takes into account the quantum effects of confinement, with particular focus on HHG and ionization in quantum wires. We then present results that show how the extent of this confinement affects the ionization and the harmonic spectrum.

Outline

In the first part of this thesis, we will develop a two-band model for high harmonic generation in confined quantum systems in general, with special focus on quantum wires. Chapter 1 will provide the theoretical background for HHG in bulk solids, the framework on which our theory for HHG in confined systems will be built. In this chapter, the Hamiltonian of the solid-state system in the presence of an external field is defined neglecting electron-electron interaction, and the time-dependent Schrödinger equation (TDSE) is solved using a Bloch expansion of the wavefunction, according to the approach of Refs. [28, 29]. We simplify the equations of motion using the two band model [37] and derive a set of differential equations for the probability amplitudes. We then show how we calculate obervable quantities of interest, namely the interband and intraband currents.

The second chapter builds on the methods described in the first by introducing a confining potential to the Hamiltonian used for bulk crystals. To do this, we first solve the eigenvalue equation for this system with a general confining potential and expand the wavefunction in the basis of the new eigenvectors instead. Next, we derive equations of motion for confined systems in general and apply it to the case of a quantum wire, simplifying our equations accordingly. Finally, we discuss how to calculate the relevant observables.

In the Results and Discussions part of this thesis we numerically investigate ionization and HHG in a quantum wire. Different wire widths are examined and compared to the results from bulk calculations. We find that the overall harmonic intensities of both contributions are suppressed when the quantum wire is made narrower. Investigating further we find that this is due to lower final ionisation (ionisation at end of pulse). For strong field applications to solids, a lower ionisation means a higher damage threshold. Thus we are able to control the damage threshold of the wire by changing its width, which could prove particularly useful for realizing all-solid-state electron accelerators [38].

Part I

Theory

Chapter 1

High Harmonic Generation in Solids

Here we will present the theoretical background for HHG in bulk solids. This will provide the framework on which our theory for HHG in confined quantum systems will be built. To do this we follow the approach outlined in Refs [28, 29] by deriving the equations of motion for electron and hole dynamics for a two band single-electron model [37] (i.e, electron-electron interaction is neglected). The time-dependent Schrodinger equation (TDSE) will be solved by representing the wavefunction in the basis of Bloch functions [31, 32]. This will yield equations of motion for the probability amplitudes of the valence and conduction bands. From the time integration of these equations we can obtain the quantities of interest, namely the interband and intraband currents, as well as the band populations and polarization.

1.1 The Hamiltonian of the system

Throughout this chapter and the rest of this thesis, unless otherwise noted, we shall use atomic units where $m_e = e = \hbar = 1$. In these units the Schrödinger equation is

$$i|\dot{\Psi(t)}\rangle = (H_0 + H_{int})\,|\Psi(t)\rangle \tag{1.1}$$

where we model the Hamiltonian as a sum of two contributions: the unperturbed Hamiltonian, H_0 of an infinite solid (or one with a very large number of lattice points), and the interaction with the laser pulse, H_{int}. The solid or Bloch Hamiltonian is

$$H_0 = -\nabla^2 + U(\mathbf{r}) \tag{1.2}$$
$$\tag{1.3}$$

The potential $U(\mathbf{r})$ is the sum of potentials due to each lattice point. Since every lattice point is identical to any other, this has to be periodic in space:

$$U(\mathbf{r} + \mathbf{R}) = U(\mathbf{r}). \tag{1.4}$$

Here $\mathbf{R}$ is any direct lattice vector [31], which means if the position of a lattice point is translated by $\mathbf{R}$, it will give the position of another lattice point. When the driving field frequency is low, so that its wavelength is much greater than the lattice constants, the **dipole approximation** can be used to write the interaction Hamiltonian as $H_{int} = -\mathbf{r} \cdot \mathbf{F}(t)$, where $\mathbf{F}$ is constant in space. The total Hamiltonian of the system

will then be the sum of the unperturbed lattice Hamiltonian and the Hamiltonian of the applied electric field, which we denote as

$$\begin{aligned} H &= H_0 + H_{int} \\ &= -\nabla^2 + U(\mathbf{r}) - \mathbf{r} \cdot \mathbf{F}. \end{aligned} \tag{1.5}$$

Bloch Eigenstates

The eigenfunctions of the unperturbed Hamiltonian (1.2) are Bloch states which satisfy the eigenvalue equation

$$H_0 \left|\Phi_{m,\mathbf{k}}\right\rangle = E_{m,\mathbf{k}} \left|\Phi_{m,\mathbf{k}}\right\rangle \tag{1.6}$$

where $|\Phi_{m,\mathbf{k}}\rangle$ is a Bloch eigenstate, $E_{m,\mathbf{k}}$ is its corresponding eigenvalue. The band index is denoted by 'm', and $\mathbf{k}$ is known as the **crystal momentum** or Bloch wave vector, which is a vector in the reciprocal lattice [31]. Because of translational symmetry, the wave vector can be restricted to the *first Brillouin zone* (denoted as BZ), which is a primitive cell of the reciprocal lattice centered around $\mathbf{k} = 0$. Any wavefunction in this system can be expressed in terms of the bands m, and wavevectors $\mathbf{k} \in BZ$, which for a cubic lattice implies

$$k_i < \frac{2\pi}{a_i} \tag{1.7}$$

where a_i are the lattice constants in directions $i = x, y, z$. The $\mathbf{r}$-basis representation of the Bloch state is

$$\Phi_{m,\mathbf{k}}(\mathbf{r}) = u_{m,\mathbf{k}}(\mathbf{r}) e^{i\mathbf{k}\cdot\mathbf{r}}, \tag{1.8}$$

where

$$\Phi_{m,\mathbf{k}}(\mathbf{r}) = \langle \mathbf{r} | \Phi_{m,\mathbf{k}} \rangle \,. \tag{1.9}$$

Here $u_{m,\mathbf{k}}(\mathbf{r})$ is any periodic function that has the same periodicity as the direct lattice, i.e,

$$u_{m,\mathbf{k}}(\mathbf{r} + \mathbf{R}) = u_{m,\mathbf{k}}(\mathbf{r}). \tag{1.10}$$

Properties of Bloch states

Bloch states satisfy orthonormality, i.e,

$$\langle \Phi_{m,\mathbf{k}} | \Phi_{m',\mathbf{k}'} \rangle = \int_L \Phi^*_{m,\mathbf{k}}(\mathbf{r}) \Phi_{m',\mathbf{k}'}(\mathbf{r}) d^3r \tag{1.11}$$

$$= \delta_{m,m'} \delta_{k,k'} \tag{1.12}$$

For $\mathbf{k} = \mathbf{k}'$, we also have an orthonormality relationship for $u_{m,\mathbf{k}}$ given by

$$\langle \Phi_{m,\mathbf{k}} | \Phi_{m',\mathbf{k}} \rangle = \langle u_{m,\mathbf{k}} | u_{m',\mathbf{k}} \rangle = \delta_{m,m'} \tag{1.13}$$

The symbol $\delta_{x,x'}$ stands for the **Kronecker Delta Function**, which has value 1 if $x = x'$, 0 otherwise. Bloch states also satisfy completeness:

$$\sum_{m,\mathbf{k}\in BZ} |\Phi_{m,\mathbf{k}}\rangle \langle\Phi_{m,\mathbf{k}}| = I \tag{1.14}$$

where I is the identity operator.
Since the unperturbed Hamiltonian, H_0, is diagonal in this basis, we shall use this basis to represent our wave-function. The other terms in the total Hamiltonian can also be simplified in this basis given certain conditions, as we shall discuss in the next section.

1.2 Equations of motion

Now that we have a suitable basis for our problem, we can proceed to solving the Schrödinger equation following the methods of Ref. [29]; however, here we will work with the probability amplitudes as opposed to the density matrix equations. We first expand the wavefunction $\Psi(\mathbf{r}, t)$ in the Bloch-eigenstate basis:

$$|\Psi(t)\rangle = \sum_{m,\mathbf{k}} a_{m,\mathbf{k}}(t) |\Phi_{m,\mathbf{k}}\rangle. \tag{1.15}$$

We can further write (1.15) in the $\mathbf{r}$-basis with components

$$\Psi(\mathbf{r}, t) = \sum_{m,\mathbf{k}} a_{m,\mathbf{k}}(t)\Phi_{m,\mathbf{k}}(\mathbf{r}) \tag{1.16}$$

$$= \sum_{m,\mathbf{k}} a_{m,\mathbf{k}}(t)u_{m,\mathbf{k}}(\mathbf{r})e^{i\mathbf{k}\cdot\mathbf{r}}. \tag{1.17}$$

Next, we insert the ansatz (1.15) in the Schrödinger equation (1.1), and obtain

$$i\sum_{m,\mathbf{k}} \dot{a}_{m,\mathbf{k}} |\Phi_{m,\mathbf{k}}\rangle = H_0 \sum_{m,\mathbf{k}} a_{m,\mathbf{k}} |\Phi_{m,\mathbf{k}}\rangle + H_{int} \sum_{m,\mathbf{k}} a_{m,\mathbf{k}} |\Phi_{m,\mathbf{k}}\rangle \tag{1.18}$$

Pre-multiplying by $\langle\Phi_{m',\mathbf{k}'}|$ yields the equation of motion for the probability amplitudes $a_{m,\mathbf{k}}$,

$$i\dot{a}_{m',\mathbf{k}'} = E_{m',\mathbf{k}'}a_{m',\mathbf{k}'} + \sum_{m,\mathbf{k}} \langle\Phi_{m',\mathbf{k}'}| H_{int} |\Phi_{m,\mathbf{k}}\rangle a_{m,\mathbf{k}} \tag{1.19}$$

$$\implies i\dot{a}_{m,\mathbf{k}} = E_{m,\mathbf{k}}a_{m,\mathbf{k}} - \mathbf{F}\cdot\sum_{m',\mathbf{k}'} \langle\Phi_{m,\mathbf{k}}| \mathbf{r} |\Phi_{m',\mathbf{k}'}\rangle a_{m',\mathbf{k}'}. \tag{1.20}$$

Equation (1.20) tells us how the probability amplitudes of the wave function evolve in time. To solve this, we need to evaluate the dipole interaction term $\langle\Phi_{m,\mathbf{k}}| \mathbf{r} |\Phi_{m',\mathbf{k}'}\rangle$.

$$\langle\Phi_{m,\mathbf{k}}| \mathbf{r} |\Phi_{m',\mathbf{k}'}\rangle = \int_{L^3} e^{-i\mathbf{k}\cdot\mathbf{r}}u^*_{m,\mathbf{k}}(\mathbf{r})\mathbf{r}u_{m',\mathbf{k}}(\mathbf{r})e^{i\mathbf{k}'\cdot\mathbf{r}}d^3r \tag{1.21}$$

where $d^3r = dxdydz$. Now, the integral above can be rewritten in a different way using the product rule identity of $\nabla_{\mathbf{k}}\Phi_{m,\mathbf{k}}$:

$$-i\nabla_{\mathbf{k}}\Phi_{m,\mathbf{k}} = -i\nabla_{\mathbf{k}}(u_{m,\mathbf{k}}e^{i\mathbf{k}\cdot\mathbf{r}}) \tag{1.22}$$

$$= -i(\nabla_{\mathbf{k}}u_{m,\mathbf{k}})e^{i\mathbf{k}\cdot\mathbf{r}} + \mathbf{r}u_{m,\mathbf{k}}e^{i\mathbf{k}\cdot\mathbf{r}} \tag{1.23}$$

Rearranging (1.23) gives

$$\mathbf{r}u_{m,\mathbf{k}}e^{i\mathbf{k}\cdot\mathbf{r}} = i(\nabla_{\mathbf{k}}u_{m,\mathbf{k}})e^{i\mathbf{k}\cdot\mathbf{r}} - i\nabla_{\mathbf{k}}\Phi_{m,\mathbf{k}}. \tag{1.24}$$

Substituting (1.24) into (1.21), we get

$$\langle\Phi_{m,\mathbf{k}}|\,\mathbf{r}\,|\Phi_{m',\mathbf{k}'}\rangle = i\int e^{-i(\mathbf{k}-\mathbf{k}')\cdot\mathbf{r}}(u^*_{m,\mathbf{k}}\nabla_{\mathbf{k}'}u_{m',\mathbf{k}'})d^3r - i\int \Phi^*_{m,\mathbf{k}}\nabla_{\mathbf{k}'}\Phi_{m',\mathbf{k}'}d^3r. \tag{1.25}$$

Here we notice that the second term on the right is:

$$i\int \Phi^*_{m,\mathbf{k}}\nabla_{\mathbf{k}'}\Phi_{m',\mathbf{k}'}d^3r = -i\nabla_{\mathbf{k}'}\langle\Phi_{m,\mathbf{k}}|\Phi_{m'\mathbf{k}'}\rangle \tag{1.26}$$

$$= -i\nabla_{\mathbf{k}'}\delta_{m,m'}\delta_{\mathbf{k},\mathbf{k}'} \tag{1.27}$$

The Kronecker delta functions on the right will eliminate all but one of the terms in the double summation in equation (1.20). For the other integral, however, we are still left with all the bands and the full Brillouin zone. To tackle this problem, we assert that non-negligible contributions only come from values of $\mathbf{k}'$ that are close to $\mathbf{k}$. In other words, $\mathbf{k}-\mathbf{k}'$ is small enough so that the exponential factor $e^{-i(\mathbf{k}-\mathbf{k}')\cdot\mathbf{r}}$ is slowly varying, and can be taken to be roughly constant over one lattice cell, i.e, for any $\mathbf{r}'$ in the primitive cell,

$$e^{-i(\mathbf{k}-\mathbf{k}')\cdot(\mathbf{n}\cdot\bar{\mathbf{a}}+\mathbf{r}')} \approx e^{-i(\mathbf{k}-\mathbf{k}')\cdot(\mathbf{n}\cdot\bar{\mathbf{a}})} \tag{1.28}$$

where for brevity we introduce the tensors

$$\mathbf{n} = (n_x, n_y, n_z) \quad ; \quad \bar{\mathbf{a}} = (\mathbf{a}_x, \mathbf{a}_y, \mathbf{a}_z) \tag{1.29}$$

and the dot operator between them is simply a vector dot product so that: $\mathbf{n}\cdot\bar{\mathbf{a}} = n_x\mathbf{a_x} + n_y\mathbf{a_y} + n_z\mathbf{a_z}$. On the other hand, the term $u^*_{m,\mathbf{k}}\nabla_{\mathbf{k}'}u_{m',\mathbf{k}'}$ is periodic and is the same for every lattice cell, that is,

$$u_{m,\mathbf{k}}(\mathbf{n}\cdot\bar{\mathbf{a}} + \mathbf{r}') = u_{m,\mathbf{k}}(\mathbf{r}') \tag{1.30}$$

Thus we can arrive at a helpful result by breaking up the integral over the entire lattice into a sum of integrals over each lattice cell, taking $e^{-i(\mathbf{k}-\mathbf{k}')\cdot\mathbf{r}}$ to be constant over each cell and pulling it out of the integral.

$$i\int_{L^3} e^{-i(\mathbf{k}-\mathbf{k}')\cdot\mathbf{r}}(u^*_{m,\mathbf{k}}\nabla_{\mathbf{k}'}u_{m',\mathbf{k}'})d^3r \tag{1.31}$$

$$= i\sum_{n_x,n_y,n_z} e^{-i(\mathbf{k}-\mathbf{k}')\cdot(\mathbf{n}\cdot\bar{\mathbf{a}})}\int_{a^3} u^*_{m,\mathbf{k}}\nabla_{\mathbf{k}'}u_{m',\mathbf{k}'}d^3r \tag{1.32}$$

The summation is a triple sum where each n_i goes from 0 to $N_i - 1$ where N_i is the number of lattice points in diretion $i = x, y$ or z. Now that we have factored the lattice integral into a sum and primitive cell integral, we evaluate the summation factor in the limit $N = N_x N_y N_z \to \infty$.

$$\sum_{n_x,n_y,n_z} e^{-i(\mathbf{k}-\mathbf{k}')\cdot(\mathbf{n}\cdot\bar{\mathbf{a}})} = \frac{1}{a^3} \sum_{n_x,n_y,n_z} e^{-i(\mathbf{k}-\mathbf{k}')\cdot(\mathbf{n}\cdot\bar{\mathbf{a}})} a^3 \tag{1.33}$$

where $a^3 = a_x a_y a_z$. In the limit $N \to \infty$, the sum becomes an integral.

$$\frac{1}{a^3} \sum_{n_x,n_y,n_z} e^{-i(\mathbf{k}-\mathbf{k}')\cdot(\mathbf{n}\cdot\bar{\mathbf{a}})} a^3 = \frac{1}{a^3} \int_{L^3} e^{-i(\mathbf{k}-\mathbf{k}')\cdot(\mathbf{n}\cdot\bar{\mathbf{a}})} dr^3 \tag{1.34}$$

The integral must be zero for any of the allowed values of $\mathbf{k}$ and $\mathbf{k}'$ unless $\mathbf{k} = \mathbf{k}'$ because of the Born-von Karman periodic boundary conditions imposed on the entire lattice [31]. For $\mathbf{k} = \mathbf{k}'$ the integral is L^3.

$$\therefore \quad i \int_{L^3} e^{-i(\mathbf{k}-\mathbf{k}')\cdot\mathbf{r}} (u^*_{m,\mathbf{k}} \nabla_{\mathbf{k}'} u_{m',\mathbf{k}'}) d^3r \tag{1.35}$$

$$= i\delta_{\mathbf{k},\mathbf{k}'} \frac{L^3}{a^3} \int_{a^3} u^*_{m,\mathbf{k}} \nabla_{\mathbf{k}'} u_{m',\mathbf{k}'} d^3r \tag{1.36}$$

$$= i\delta_{\mathbf{k},\mathbf{k}'} \int_{L^3} u^*_{m,\mathbf{k}} \nabla_{\mathbf{k}'} u_{m',\mathbf{k}'} d^3r \tag{1.37}$$

$$= \mathbf{d}_{m,m'}(\mathbf{k}) \delta_{\mathbf{k},\mathbf{k}'} \tag{1.38}$$

Here we used the fact that $N = \frac{L^3}{a^3}$ and because $u_{m,\mathbf{k}}$ is periodic over the primitive cell, the integral of such a periodic function over the entire lattice is simply N times the integration of one primitive cell. We call $\mathbf{d}_{m,m'}(\mathbf{k}) = \int_{L^3} u^*_{m,\mathbf{k}} \nabla_{\mathbf{k}'} u_{m',\mathbf{k}} d^3r$ the **transition dipole moment**, which is dependent on interband transitions only, i.e,

$$\mathbf{d}_{m,m'}(\mathbf{k}) = 0 \quad \text{if} \quad m = m' \tag{1.39}$$

The reason for this and a derivation of its value using the $\mathbf{k} \cdot \mathbf{p}$ theory [32] is given in Appendix B. Combining equations (1.27),(1.38) and (1.39), we get

$$\langle \Phi_{m,\mathbf{k}} | \, \mathbf{r} \, | \Phi_{m',\mathbf{k}'} \rangle = -i\nabla_{\mathbf{k}'} \delta_{m,m'} \delta_{\mathbf{k},\mathbf{k}'} + \mathbf{d}_{m,m'\neq m}(\mathbf{k}) \delta_{\mathbf{k},\mathbf{k}'} \tag{1.40}$$

Now we substitute our final form for the dipole moment given by (1.40) into the Schrödinger equation for $a_{m,\mathbf{k}}(t)$ given by (1.20).

$$\begin{aligned} i\dot{a}_{m,\mathbf{k}} &= E_{m,\mathbf{k}} a_{m,\mathbf{k}} - \sum_{m',\mathbf{k}'} (-i\nabla_{\mathbf{k}'} \delta_{m,m'} \delta_{\mathbf{k},\mathbf{k}'} + \mathbf{d}_{m,m'\neq m}(\mathbf{k}) \delta_{\mathbf{k},\mathbf{k}'}) \cdot \mathbf{F} a_{m',\mathbf{k}'} \\ &= E_{m,\mathbf{k}} a_{m,\mathbf{k}} + i\mathbf{F} \cdot \nabla_{\mathbf{k}} a_{m,\mathbf{k}} - \mathbf{F} \cdot \sum_{m'} \mathbf{d}_{m,m'\neq m}(\mathbf{k}) a_{m',\mathbf{k}}. \end{aligned} \tag{1.41}$$

And so the Scrödinger equation for $a_{m,\mathbf{k}}(t)$ with the dipole approximation reads

$$\dot{a}_{m,\mathbf{k}} = (-iE_{m,\mathbf{k}} + \mathbf{F}\cdot\nabla_{\mathbf{k}})a_{m,\mathbf{k}} + i\mathbf{F}\cdot\sum_{m'\neq m}\mathbf{d}_{m,m'}(\mathbf{k})a_{m',\mathbf{k}} \tag{1.42}$$

The integration of equation (1.42) is complicated by the presence of the $\nabla_{\mathbf{k}}$ term, but we can eliminate it and simplify the equation by a transformation of variables,

$$\kappa(\mathbf{k},\mathbf{t}) = \mathbf{k} - \mathbf{A}(t) \tag{1.43}$$

and

$$\tau(\mathbf{k},t) = t \tag{1.44}$$

where the vector potential $\mathbf{A}(t)$ is defined as

$$\frac{d\mathbf{A}(t)}{dt} = -\mathbf{F}(t) \tag{1.45}$$

Note that this also shifts the Brilouin zone to $BZ' = BZ - \mathbf{A}(t)$. These transformations lead to the following rules for derivatives, for a given function $f(\mathbf{k},t)$ tranformed to $f(\kappa,\tau)$:

$$\begin{aligned}\frac{df(\kappa,\tau)}{dt} &= \frac{\partial f(\kappa,\tau)}{\partial\kappa}\frac{d\kappa}{dt} + \frac{\partial f(\kappa,\tau)}{\partial\tau}\frac{d\tau}{dt}\\ &= \frac{\partial f(\kappa,\tau)}{\partial\kappa}\mathbf{F} + \frac{\partial f(\kappa,\tau)}{\partial\tau}\\ &= \left(\mathbf{F}\frac{\partial}{\partial\kappa} + \frac{\partial}{\partial\tau}\right)f(\kappa,\tau)\end{aligned} \tag{1.46}$$

and

$$\begin{aligned}\frac{df(\kappa,\tau)}{d\mathbf{k}} &= \frac{\partial f(\kappa,\tau)}{\partial\kappa}\frac{d\kappa}{d\mathbf{k}} + \frac{\partial f(\kappa,\tau)}{\partial\tau}\frac{d\tau}{d\mathbf{k}}\\ &= \frac{\partial f(\kappa,\tau)}{\partial\kappa}\end{aligned} \tag{1.47}$$

Now we apply the transformation to the probability amplitude equation (1.42) and subsequently eliminate $\nabla_{\mathbf{k}}$.

$$\frac{da_{m,\kappa}(t)}{dt} = \{-iE_m(\kappa+\mathbf{A}) + \mathbf{F}\cdot\nabla_{\mathbf{k}}\}a_{m,\kappa} + i\mathbf{F}\cdot\sum_{m'\neq m}\mathbf{d}_{m,m'}(\kappa+\mathbf{A})a_{m',\kappa}$$

$$\Rightarrow \frac{\partial a_{m,\kappa}}{\partial\tau} + \cancel{\mathbf{F}\cdot\nabla_\kappa a_{m,\kappa}} = -iE_m(\kappa+\mathbf{A})a_{m,\kappa} + \cancel{\mathbf{F}\cdot\nabla_\kappa a_{m,\kappa}} + i\mathbf{F}\cdot\sum_{m'\neq m}\mathbf{d}_{m,m'}(\kappa+\mathbf{A})a_{m',\kappa}$$

Thus the equation for amplitudes in terms of the transformed variables is given by (replacing τ with t)

$$\partial_t a_{m,\kappa}(t) = -iE_m\big(\kappa+\mathbf{A}(t)\big)a_{m,\kappa}(t) + i\mathbf{F}(t)\cdot\sum_{m'\neq m}\mathbf{d}_{m,m'}\big(\kappa+\mathbf{A}(t)\big)a_{m',\kappa}(t) \tag{1.48}$$

where $\partial_t = \frac{\partial}{\partial t}$. The ordinary differential equation (1.48) can be further simplified by

another transformation using an integrating factor:

$$a_{m,\kappa}(t) = b_{m,\kappa}(t) \exp\left[-i \int_{-\infty}^{t} E_m(\kappa + \mathbf{A}(t'))dt'\right]. \tag{1.49}$$

Here we write the amplitude as a product of a transformed amplitude and a phase factor $\exp\left[-i \int_{-\infty}^{t} E_m(\kappa + \mathbf{A}(t'))dt'\right]$. Calculating the time derivative of the above and rearranging, we get

$$\partial_t b_{m,\kappa}(t) e^{-i\int_{-\infty}^{t} E_{m'}(\kappa+\mathbf{A}(t'))dt'} = \partial_t a_{m,\kappa}(t) + iE_m(\kappa + \mathbf{A}(t'))a_{m,\kappa}(t) \tag{1.50}$$

Substituting in the expression for $\partial_t a_{m,\kappa}(t)$ from (1.48) and replacing $a_{m,\kappa}$ with (1.49), we obtain the following equation for $\partial_t b_{m,\kappa}(t)$:

$$\begin{aligned}
\partial_t b_{m,\kappa} &= i\mathbf{F} \cdot \sum_{m' \neq m} \mathbf{d}_{m,m'} b_{m,\kappa} e^{-i\int_{-\infty}^{t} E_{m'}(\kappa+\mathbf{A}(t'))dt'} e^{i\int_{-\infty}^{t} E_m(\kappa+\mathbf{A}(t'))dt'} \\
&= i\mathbf{F} \cdot \sum_{m' \neq m} \mathbf{d}_{m,m'} b_{m,\kappa} \exp\left[-i \int_{-\infty}^{t} \Delta E_{m'm}(\kappa + \mathbf{A}(t'))dt'\right]
\end{aligned} \tag{1.51}$$

where $\Delta E_{m'm} = E_{m'} - E_m$

In the two band model, we just have a conduction band ($m = c$) and a valence band ($m = v$). The band gap between the two bands is defined as $E_g = \Delta E_{c'v} = E_c - E_v$. Equation (1.51) then becomes

$$\partial_t b_{c,\kappa} = i\mathbf{F} \cdot \mathbf{d}^*(\kappa + \mathbf{A}(t))b_{v,\kappa} \exp[iS] \tag{1.52}$$

$$\partial_t b_{v,\kappa} = i\mathbf{F} \cdot \mathbf{d}(\kappa + \mathbf{A}(t))b_{c,\kappa} \exp[-iS] \tag{1.53}$$

Here, $S = \int_{-\infty}^{t} E_g(\kappa + \mathbf{A}(t'))dt'$ is the classical action. The interband dipole moment, $\mathbf{d} = \mathbf{d}_{v,c}$ and $\mathbf{d}^* = \mathbf{d}_{c,v}$, as shown below applying product rule in reverse and using the orthonormality condition for Bloch states.

$$\begin{aligned}
\mathbf{d}_{c,v} &= i \int d^3\mathbf{r} u^*_{c\mathbf{k}} \nabla_{\mathbf{k}} u_{v\mathbf{k}} \\
&= i\nabla_{\mathbf{k}} \int d^3\mathbf{r} u^*_{c\mathbf{k}} u_{v\mathbf{k}} - i \int d^3\mathbf{r} u_{v\mathbf{k}} \nabla_{\mathbf{k}} u^*_{c\mathbf{k}} \\
&= \mathbf{d}^*_{v,c}
\end{aligned} \tag{1.54}$$

1.3 Currents and harmonic spectra

Numerically solving equations (1.52) and (1.53) give us $b_{m,\kappa}(t)$ or $a_{m,\kappa}(t)$. From these we can calculate the time-dependent band population,

$$n_m = |a_m|^2 = |b_m|^2 \tag{1.55}$$

Where κ and t have been suppressed for brevity. The **intraband current** is due to the motion of an electron or hole within a single band. This is calculated as

$$\mathbf{j}_{ra}(t) = \sum_{m=c,v} \int_{BZ'} \mathbf{v}_m(\kappa + \mathbf{A}(t)) n_m(\kappa, t) d^3\kappa, \tag{1.56}$$

where $BZ' = BZ - \mathbf{A}(t)$ and

$$\mathbf{v}_m(\mathbf{k}) = \nabla_{\mathbf{k}} E_m(\mathbf{k}) \tag{1.57}$$

is the band velocity, or group velocity of an electron in band m, obtained from the dispersion relationship of the band structure. The polarization is due to band transitions and is calculated as

$$\mathbf{p}(\kappa, t) = \mathbf{d}(\kappa + \mathbf{A}(t)) a^*_{c,\kappa} a_{v,\kappa} + c.c. \tag{1.58}$$

$$= \mathbf{d}(\kappa + \mathbf{A}(t)) \pi(\kappa, t) \exp[iS(\kappa, t)] + c.c.. \tag{1.59}$$

where $\pi(\kappa, t) = b^*_{c,\kappa} b_{v,\kappa}$ The interband current, caused by transition of electrons across the two bands, can be defined as the rate of change of the total polarization:

$$\mathbf{j}_{er}(t) = \frac{d}{dt} \int_{BZ'} \mathbf{p}(\kappa, t) d^3\kappa \tag{1.60}$$

Finally, the harmonic spectrum is obtained by taking the Fourier transform of the current:

$$\text{Interband spectrum :} \quad |\tilde{\mathbf{j}}_{er}(\omega)|^2 = |\mathscr{F}[\mathbf{j}_{er}(t)]|^2 \tag{1.61}$$

$$\text{Intraband spectrum :} \quad |\tilde{\mathbf{j}}_{ra}(\omega)|^2 = |\mathscr{F}[\mathbf{j}_{ra}(t)]|^2 \tag{1.62}$$

1.4 Saddle-point analysis and 3-step model

An intuitive understanding of HHG in solids can be achieved by using the Keldysh appoximation [39], in which the depletion of the valence band is assumed to be negligible. In other words, the total valence band population

$$\int_{BZ} n_v(\mathbf{k}, t) d^3\mathbf{k} \approx 1 \tag{1.63}$$

Since every $\mathbf{k}$ in the valence band is initially occupied, normalization demands that the valence band probability amplitude be

$$b_v(\mathbf{k}, t) \approx \frac{1}{K^{\frac{3}{2}}} \tag{1.64}$$

where $K^3 = K_x K_y K_z$ with K_i being the Brillouin zone length in the i^{th} direction. This decouples our equation for b_c, making Eqn. (1.52) integrable, i.e,

$$b_{c,\kappa}(t) = \frac{i}{K^{\frac{3}{2}}} \int_{-\infty}^{t} dt' \mathbf{F}(t') \cdot \mathbf{d}^*(\kappa + \mathbf{A}(t')) \exp[iS(\kappa, t')] \tag{1.65}$$

The derivation of the intraband current in this approximation is given in Vampa

et al. (2014) [29]. Here we present just the interband current, which is found to be the dominating mechanism for higher harmonics [22, 29]. Substituting (1.65) into the polarization (Eqn. 1.59), we arrive at the following expression for the interband current:

$$\tilde{\mathbf{j}}_{er}(\omega) = \frac{\omega}{K^{\frac{3}{2}}} \int_{BZ} d^3\mathbf{k} \mathbf{d}(\mathbf{k}) \int_{-\infty}^{\infty} dt e^{-i\omega t} \int_{-\infty}^{t} dt' F(t') d^*(\mathcal{K}_{t'}) \exp[-iS(\mathbf{k}, t', t)] \tag{1.66}$$

$$\tag{1.67}$$

where $\mathcal{K}_{t'} = \mathbf{k} + \mathbf{A}(t') - \mathbf{A}(t)$ and $S(\mathbf{k}, t', t) = \int_{t'}^{t} E_g(\mathcal{K}_\tau) d\tau$ and the Brillouin zone has been shifted back to the original.

Equation (1.66) can be solved by saddle-point integration. The dominant contribution to the integral occurs when the saddle-point conditions are met, and these are found to be

$$\nabla_{\mathbf{k}} S = \Delta\mathbf{x}_c - \Delta\mathbf{x}_v = 0 \tag{1.68}$$

$$\frac{dS}{dt'} = E_g[\mathbf{k} - \mathbf{A}(t) + \mathbf{A}(t')] = 0 \tag{1.69}$$

$$\frac{dS}{dt} = E_g(\mathbf{k}) = \omega \tag{1.70}$$

where $\Delta\mathbf{x}_m = \int_{t'}^{t} \mathbf{v}_m(\tau) d\tau = \mathbf{x}_m(t) - \mathbf{x}_m(t')$ is the net displacement of the electron/hole in band m between its time of birth due to ionization (t'), and the time of observation (t). Thus, the first saddle-point condition states that non-neglible contributions to HHG occur only when electrons and holes recombine after being ionized and accelerated by the field. This mirrors the condition in atoms that electrons must recollide with ions for HHG to occur [2, 3].

Equation(1.69) states that $\mathbf{k} - \mathbf{A}(t) + \mathbf{A}(t')$ must be such that E_g is zero. Since E_g is not zero for any real value of $\mathbf{k}$, the solution must be that $\mathbf{k}$ be complex. However, since E_g is approximately sinusoidal (see Chapter 3, Table 3.1), to meet this condition the real part of $\mathbf{k} - \mathbf{A}(t) + \mathbf{A}(t')$ must be zero, which implies that at the time of birth

$$\mathrm{Re}\{\mathbf{k}\} = \mathrm{Re}\{\mathbf{A}(t') - \mathbf{A}(t')\} = 0 \tag{1.71}$$

that is, the electron and hole must be born with zero crystal momentum for HHG to occur. This is in accordance with the atomic case where the electron is born in the continuum with zero initial velocity.

Last of all, equation (1.70) is a statement of conservation of energy that tells us that the emitted photon will have an angular frequency ω with an energy equal to that of the bandgap at the crystal momentum $\mathbf{k}$ at which the recollision occurs. This gives us a maximum cut-off harmonic for the interband harmonic given by the maximum band gap of the solid. These conditions provide us with a physical picture similar to the three-step model in atoms [2, 3].

With this we conclude the chapter on solids that lays out the basic framework for the study of HHG in crystal structures. In the next chapter we shall extend this theory to include a confining potential. This will allow for the investigation of confined quantum systems such as quantum wires.

Chapter 2

High Harmonic Generation in Quantum Wires

A quantum wire is a confined quantum system where the electron motion is restricted in two spatial dimensions by a confining potential. Electron motion in the remaining direction is unimpeded, thus creating an effective one dimensional system. Here we extend the theory for bulk solids, presented in the previous chapter, to systems in which there is an additional confining potential V. We examine the case of a quantum wire, but the formalism we present can also be applied to other confined quantum systems.

2.1 Quantum wire Hamiltonian

In the absence of an external electric field, the Hamiltonian is given by,

$$H_q = H_0 + V \tag{2.1}$$

where $H_0 = -\nabla^2 + U$ is the bulk Hamiltonian, satisfying Equation (1.6). The total time dependent Hamiltonian is then

$$H(t) = H_q + H_{int}, \tag{2.2}$$

where $H_{int} = \mathbf{r} \cdot \mathbf{F}(t)$. Our approach here will be to solve the eigenvalue equation for H_q, similar to what we did in the last chapter, then proceed with the derivation using the new eigenvalues and states.

The eigenvalue equation for the new Hamiltonian is

$$H_q \left|\psi_\eta\right\rangle = \varepsilon_\eta \left|\psi_\eta\right\rangle \tag{2.3}$$

Here, ε_η is the η^{th} eigenvalue, corresponding to the η^{th} eigenvector, ψ_η. If we want to retain the simplicity of the previous derivation for the bulk Hamiltonian, we need to keep working in the Bloch basis. So we expand the eigenstates ψ_η in the Bloch basis:

$$\left|\psi_\eta\right\rangle = \sum_\kappa \left|\Phi_\kappa\right\rangle \left\langle\Phi_\kappa|\psi_\eta\right\rangle \tag{2.4}$$

$$= \sum_\kappa \alpha_{\eta,\kappa} \left|\Phi_\kappa\right\rangle \tag{2.5}$$

where $\alpha_{\eta,\kappa} = \langle \Phi_\kappa | \psi_\eta \rangle$. For brevity, κ is meant to imply $m, \mathbf{k} \in BZ$. Now, we substitute the expression (2.5) into equation (2.3) and expand H_q as $H_0 + V$ to get

$$\sum_\kappa \alpha_{\eta,\kappa} H_0 \left|\Phi_\kappa\right\rangle + \sum_\kappa \alpha_{\eta,\kappa} V \left|\Phi_\kappa\right\rangle = \varepsilon_\eta \sum_\kappa \alpha_{\eta,\kappa} \left|\Phi_\kappa\right\rangle . \tag{2.6}$$

Premultipling with $\langle \Phi_\kappa |$ and utilising orthonormality of Bloch states gives

$$\varepsilon_\eta \alpha_{\eta,\kappa} = \alpha_{\eta,\kappa} E_\kappa + \sum_{\kappa'} \alpha_{\eta,\kappa'} \left\langle \Phi_\kappa \right| V \left|\Phi_{\kappa'}\right\rangle . \tag{2.7}$$

Potential in Bloch basis

In equation (2.7) we now evaluate the matrix elements of V in the Bloch basis:

$$\left\langle \Phi_\kappa \right| V \left|\Phi_{\kappa'}\right\rangle = \int_{L^3} u^*_\kappa(\mathbf{r}) e^{-i\mathbf{k}\cdot\mathbf{r}} V(\mathbf{r}) u_{\kappa'}(\mathbf{r}) e^{i\mathbf{k}'\cdot\mathbf{r}} d^3r \tag{2.8}$$

$$= \int_{L^3} u^*_\kappa(\mathbf{r}) V(\mathbf{r}) u_{\kappa'}(\mathbf{r}) e^{-i(\mathbf{k}-\mathbf{k}')\cdot\mathbf{r}} d^3r \tag{2.9}$$

where L^3 denotes integration over the entire lattice. We now assume a slowly varying (in space) potential that varies very little within a lattice cell, where the $u_{\kappa'}(\mathbf{r})$ factors are periodic. Following a similar argument to that of Section 1.2, the exponential factor $e^{-i(\mathbf{k}-\mathbf{k}')\cdot\mathbf{r}}$ will render the integral negligibly small except for $|\mathbf{k}' - \mathbf{k}| \ll |\mathbf{K_b}|$ where $\mathbf{K_b}$ is wave vector on the edge of the Brillouin zone. With this case in point, we can make use of the **$\mathbf{k}\cdot\mathbf{p}$ approximation** (see Appendix B) to expand the Bloch function around a reciprocal lattice vector $\mathbf{K}$ and neglect the $\mathbf{k}$-dependence of the periodic function $u_{m,\mathbf{k}}$, i.e,

$$\mathbf{k} = \mathbf{K} + \Delta\mathbf{k} \quad ; \quad \mathbf{k}' = \mathbf{K} + \Delta\mathbf{k}' \tag{2.10}$$

$$\Phi_{m,\mathbf{k}} \approx u_{m,\mathbf{K}} e^{im\mathbf{K}} e^{im\Delta\mathbf{k}}. \tag{2.11}$$

Substituting (2.10) and (2.11) into (2.9) and reintroducing the band index m,

$$\left\langle \Phi_{m,\mathbf{k}} \right| V \left|\Phi_{m',\mathbf{k}'}\right\rangle \approx \int_{L^3} u^*_{m,\mathbf{K}}(\mathbf{r}) u_{m',\mathbf{K}}(\mathbf{r}) V(\mathbf{r}) e^{i(\Delta\mathbf{k}'-\Delta\mathbf{k})\cdot\mathbf{r}} d^3r. \tag{2.12}$$

Now, just like in Sec.(1.2), we use a slowly varying approximation for the potential so that it is roughly constant in one primitive cell, that is,

$$V(\mathbf{r} + \mathbf{a}_i) \approx V(\mathbf{r}) \tag{2.13}$$

where $\mathbf{a}_i$ is a primitive lattice vector. Alternatively we can write the potential as

$$V(\mathbf{r}) = V(\mathbf{n}\cdot\bar{\mathbf{a}} + \mathbf{r}') \approx V(\mathbf{n}\cdot\bar{\mathbf{a}}) \tag{2.14}$$

where $\mathbf{r}'$ is any vector within the primitive cell; $\bar{\mathbf{a}}$ and $\mathbf{n}$ are defined in Eqn.(1.29). We can now write our integration over the whole lattice following the recipe of Sec.(1.2).

$$\int_{L^3} e^{i(\Delta\mathbf{k}'-\Delta\mathbf{k})\cdot\mathbf{r}} u^*_{m,\mathbf{k}} V(\mathbf{r}) u_{m',\mathbf{k}'} d^3r \tag{2.15}$$

$$= \sum_{n_x,n_y,n_z} e^{i(\Delta\mathbf{k}'-\Delta\mathbf{k})\cdot(\mathbf{n}\cdot\bar{\mathbf{a}})} V(\mathbf{n}\cdot\bar{\mathbf{a}}) \int_{a^3} u^*_{m,\mathbf{K}} u_{m',\mathbf{K}} e^{i(\Delta\mathbf{k}'-\Delta\mathbf{k})\cdot\mathbf{r}} d^3r \tag{2.16}$$

where L^3 denotes integration over the entire lattice, and a^3 over a primitive cell.

Since $|\Delta\mathbf{k}'-\Delta\mathbf{k}| \ll |\mathbf{K_b}|$, the integral on the right can be approximated as $\int_{a^3} u^*_{m,\mathbf{K}} u_{m',\mathbf{K}} d^3r$, which is nothing but $\frac{1}{N}\langle\Phi_{m,\mathbf{K}}|\Phi_{m',\mathbf{K}}\rangle = \frac{1}{N}\delta_{m,m'}$, where $N = N_xN_yN_z$ is the total number of lattice points. Thus,

$$\langle\Phi_{m,\mathbf{k}}| V |\Phi_{m',\mathbf{k}'}\rangle = \delta_{m,m'}\frac{1}{N}\sum_{n_x,n_y,n_z} e^{i(\Delta\mathbf{k}'-\Delta\mathbf{k})\cdot(\mathbf{n}\cdot\bar{\mathbf{a}})} V(\mathbf{n}\cdot\bar{\mathbf{a}}) \tag{2.17}$$

$$= \delta_{m,m'}\frac{1}{L^3}\sum_{n_x,n_y,n_z} e^{i(\Delta\mathbf{k}'-\Delta\mathbf{k})\cdot(\mathbf{n}\cdot\bar{\mathbf{a}})} V(\mathbf{n}\cdot\bar{\mathbf{a}}) a^3 \tag{2.18}$$

$$= \delta_{m,m'}\frac{1}{L^3}\int_{L^3} e^{i(\Delta\mathbf{k}'-\Delta\mathbf{k})\cdot\mathbf{r}} V(\mathbf{r}) d^3r \tag{2.19}$$

which happens to be the Fourier transform of $V(\mathbf{r})$, thus

$$\langle\Phi_{m,\mathbf{k}}| V |\Phi_{m',\mathbf{k}'}\rangle = \delta_{m,m'}\mathscr{F}[V(\mathbf{r})](\Delta\mathbf{k}'-\Delta\mathbf{k}) \tag{2.20}$$

where $\mathscr{F}$ is the Fourier transform operator.

2.2 Separable band structure and potential

To simplify the computation of the new eigenvalues we note that the band structure for the m^{th} band can be written as the sum of the bands along each individual axis, i.e,

$$E_m(\mathbf{k}) = E_{m,x}(k_x) + E_{m,y}(k_y) + E_{m,z}(k_z) \tag{2.21}$$

This form of band-structure is commonly used in solid state physics [28, 29, 40, 41]. This must be due to the fact that the bulk Hamiltonian $H_0 = H_{0x} + H_{0y} + H_{0z}$ is separable (i.e, the atomic potential used in the band structure calculation is separable). Thus by adding a confining potential of the form

$$V(\mathbf{r}) = V_x(x) + V_y(y) + V_z(z), \tag{2.22}$$

we can separate the 3D eigenvalue equation (2.7) into one-dimensional equations. To do this, we first write the quantum wire Hamiltonian as

$$H_q = H_{qx} + H_{qy} + H_{qz} \tag{2.23}$$

where $H_{qi} = H_{0i} + V_i$ for $i = x, y, z$. This means we can write eigenstates $|\psi_\eta\rangle$ as a tensor product of 1D wavefunctions,

$$|\psi_\eta\rangle = |\psi_{\eta_x}\rangle \otimes \left|\psi_{\eta_y}\right\rangle \otimes |\psi_{\eta_z}\rangle\,, \tag{2.24}$$

each of which has a corresponding eigenvalue ε_{η_x}, ε_{η_y} and ε_{η_z}. As the eigenvalues $E_m(\mathbf{k})$ of the bulk hamiltonian H_0 are also separable, the Bloch eigenstates of H_0 can be taken to be separable as well, so that

$$|\Phi_\kappa\rangle = |\Phi_{\kappa_x}\rangle \otimes \left|\Phi_{\kappa_y}\right\rangle \otimes |\Phi_{\kappa_z}\rangle \tag{2.25}$$

where κ_i is m, k_i. We take the projection of the eigen value equation (2.3) on the Bloch basis, and expand $\langle\Phi_\kappa| H_q |\psi_\eta\rangle$ as

$$\langle\Phi_{k_x}| H_{qx} |\psi_{\eta_x}\rangle \alpha_y\alpha_z + \left\langle\Phi_{k_y}\right| H_{qy} \left|\psi_{\eta_y}\right\rangle \alpha_x\alpha_z + \langle\Phi_{k_z}| H_{qx} |\psi_{\eta_z}\rangle \alpha_x\alpha_y \tag{2.26}$$

where $\alpha_i = \alpha_{\eta_i,\kappa_i} = \langle\Phi_\kappa|\psi_\eta\rangle$. We then expand $\varepsilon_\eta \langle\Phi_\kappa|\psi_\eta\rangle$ as

$$(\varepsilon_{\eta_x} + \varepsilon_{\eta_y} + \varepsilon_{\eta_z})\alpha_x\alpha_y\alpha_z$$

Equating the two, dividing through by $\alpha_x\alpha_y\alpha_z$ and rearranging gives

$$\left(\frac{W_x}{\alpha_x} - \varepsilon_{\eta_x}\right) + \left(\frac{W_y}{\alpha_y} - \varepsilon_{\eta_y}\right) + \left(\frac{W_z}{\alpha_z} - \varepsilon_{\eta_z}\right) = 0 \tag{2.27}$$

where $W_i = \langle\Phi_{k_i}| H_{qi} |\psi_{n,i}\rangle$ for $i = x, y, z$.

Eqn.(2.27) is a sum of independent terms equating to 0, so each term must be indentically zero, i.e,

$$W_i = \alpha_i\varepsilon_{\eta_i}. \tag{2.28}$$

Furthermore, because of the $\delta_{m,m'}$ factor in Eqn.(2.20), we have two independent equations for each band, each with its own complete set of eigenstates that span the subspace of that band. We denote the i^{th} directional component of the Hamiltonian of subspace m by $W_{m,i}$, and index each solution for eigenstate ψ_m by n_i. Thus we now have a set of one-dimensional eigenvalue equations for each band given by

$$W_{m,i} = \varepsilon_{m,n_i}\alpha_{m,n_i,k_i} \tag{2.29}$$

where $i = x, y, z$ and we have reintroduced the band index m. Finally, in terms of the Bloch basis equation (2.29) reads:

$$\varepsilon_{m,n_s i}\alpha_{m,n_i,k_i} = \alpha_{m,n_i,k_i}E_{m,k_i} + \sum_{k_i'} \alpha_{m,k_i'} \left\langle\Phi_{m,k_i}\right| V_i \left|\Phi_{m,k_i'}\right\rangle. \tag{2.30}$$

2.3 Time dependent Schrödinger equation

We now proceed to our derivation of the equations of motion by solving the Schrödinger equation,

$$i\partial_t \left|\Psi(t)\right\rangle = H(t) \left|\Psi(t)\right\rangle, \tag{2.31}$$

where we expand Ψ in the Bloch basis as before:

$$\left|\Psi(t)\right\rangle = \sum_{m,\mathbf{k}} a_{m,\mathbf{k}}(t) \left|\Phi_{m,\mathbf{k}}\right\rangle \tag{2.32}$$

where $a_{m,\mathbf{k}}(t) = \langle\Phi_{m,\mathbf{k}}|\Psi(t)\rangle$. Substituting the expansion into the Schrödinger equation, and premultiplying by $\langle\Phi_{m,\mathbf{k}}|$ gives

$$i\dot{a}_{m,\mathbf{k}}(t) = \sum_{m,\mathbf{k}'} \left\langle\Phi_{m,\mathbf{k}}\right| H_q \left|\Phi_{m,\mathbf{k}'}\right\rangle a_{m,\mathbf{k}'}(t) + \sum_{m,\mathbf{k}'} \left\langle\Phi_{m,\mathbf{k}}\right| H_{int} \left|\Phi_{m,\mathbf{k}'}\right\rangle a_{m,\mathbf{k}'}(t). \tag{2.33}$$

Sine H_q is not diagonal in this basis, this equation is difficult to solve. We instead expand the wavefunction in the basis of eigenstates of H_q (Eqn. 2.3):

$$\left|\Psi(t)\right\rangle = \sum_{\eta} \beta_\eta(t) \left|\psi_\eta\right\rangle \tag{2.34}$$

where for brevity we use η to mean (m, n). Inserting this expansion in the Schrödinger equation yields

$$i\sum_{\eta} \partial_t\beta_\eta \left|\psi_\eta\right\rangle = (H_q + H_{int}) \sum_{\eta} \beta_\eta \left|\psi_\eta\right\rangle \tag{2.35}$$

$$= \sum_{\eta} \varepsilon_\eta\beta_\eta \left|\psi_\eta\right\rangle + \sum_{\eta} \beta_\eta H_{int} \left|\psi_\eta\right\rangle \tag{2.36}$$

Taking the projection on $\langle\psi_\eta|$ gives

$$i\dot{\beta}_\eta = \varepsilon_\eta\beta_\eta + \sum_{\eta'} \left\langle\psi_\eta\right| H_{int} \left|\psi_{\eta'}\right\rangle \beta_{\eta'} \tag{2.37}$$

where we used the orthonormality of the eigenstates, $\langle\psi_\eta|\psi_{\eta'}\rangle = \delta_{\eta,\eta'}$.

The difficulty with Eqn.(2.37) is the evaluation of the matrix elements of H_{int} in this new basis. In the last chapter we simplified the elements in the Bloch basis by eliminating the sum over $\mathbf{k}$. There may be a way to do something similar in this basis, but that is beyond the scope of this thesis.

A transformation to Bloch basis gives

$$\left\langle\psi_\eta\right| H_{int} \left|\psi_{\eta'}\right\rangle = \sum_{\kappa,\kappa'} \langle\psi_\eta|\Phi_\kappa\rangle \left\langle\Phi_\kappa\right| H_{int} \left|\Phi_{\kappa'}\right\rangle \langle\Phi_{\kappa'}|\psi_{\eta'}\rangle \tag{2.38}$$

$$= \sum_{\kappa,\kappa'} \alpha^*_{\eta,\kappa}\alpha_{\eta',\kappa'} \left\langle\Phi_\kappa\right| H_{int} \left|\Phi_{\kappa'}\right\rangle \tag{2.39}$$

which would give us a summation over both η and κ in the TDSE, making the computation time unfeasible. However, Eqn.(2.37) is the general equation of motion for HHG in confined systems, and in some special cases it is easily adopted into existing methodology for bulk calculations. We shall discuss this in the following sections.

2.4 Quantum wire potential and the driving field

We now define a form for the potential of a quantum wire, V. We take the axis of the wire to be parallel to $\hat{\mathbf{x}}$, so that electrons are unconfined in this direction. Furthermore, we implement V in the form of a 2D harmonic oscillator potential,

$$V(y,z) = V(y) + V(z) = \frac{1}{2}\Omega(y^2 + z^2) \tag{2.40}$$

where Ω is the angular frequency of the harmonic oscillator, which is taken to be the same in both x and y directions to emulate a wire symmetric about its axis. This potential provides an eigenvalue equation which is easily solveable, and also for which the effective mass approximation [31,32] yields an analytical solution for the eigenvalues and vectors, which is discussed in Appendix A.

In Section 2.1 we saw that

$$\langle \Phi_{m,\mathbf{k}} | \, V \, | \Phi_{m',\mathbf{k}'} \rangle = \delta_{m,m'} \mathscr{F}[V](\Delta\mathbf{k}' - \Delta\mathbf{k}). \tag{2.41}$$

Since we have separated our eigenvalue equation into a set of one-dimensional equations for each component of V, we need only work out the fourier transform of one component, say V_y, which gives

$$\mathscr{F}[\frac{1}{2}\Omega_y^2 y^2] = -\frac{1}{2}\Omega^2 \delta^{(2)}(k_y' - k_y) \tag{2.42}$$

where we have used the fact that $\Delta\mathbf{k}' - \Delta\mathbf{k} = \mathbf{k}' - \mathbf{k}$. The term on the right is the second derivative of the Dirac delta function, which can be evaluated to give us

$$\left\langle \Phi_{m,k_y} \right| V_y \left| \Phi_{m,k_y'} \right\rangle = -\frac{1}{2}\delta(k_y' - k_y)\Omega^2 \frac{\partial^2}{\partial k_y^2}. \tag{2.43}$$

Inserting this back into our eigenvalue equation (Eqn. 2.30), we get

$$\varepsilon_{m,n_y}\alpha_{m,n_y,k_y} = \alpha_{m,n_y,k_y}E_{m,k_y} - \frac{1}{2}\sum_{k_y'} \delta_{k_y,k_y'}\Omega^2 \frac{\partial^2}{\partial k_y^2}\alpha_{m,n_y,k_y'} \tag{2.44}$$

where we have replaced the Dirac delta with its discrete variant, the Kronecker delta function. Alternatively, we could have written the summation as an integral over $\mathbf{k}$. Thus for each band and direction the eigenvalue equation reads

$$\varepsilon_{m,n_i}\alpha_{m,n_i,k_i} = \alpha_{m,n_i,k_i}E_{m,k_i} - \frac{1}{2}\Omega^2 \frac{\partial^2}{\partial k_i^2}\alpha_{m,n_i,k_i} \tag{2.45}$$

where $i = y, z$. Rearranging (2.45), we get our eigenvalue equation as

$$\left[\frac{1}{2}\Omega^2\frac{\partial^2}{\partial k_i^2} - E_{m,k_i}\right]\alpha_{m,n_i,k_i} = \varepsilon_{m,n_i}\alpha_{m,n_i,k_i} \tag{2.46}$$

$$\implies \Gamma_{m,k_i}\alpha_{m,n_i,k_i} = \varepsilon_{m,n_i}\alpha_{m,n_i,k_i} \tag{2.47}$$

where $\Gamma_{m,k_i} = \frac{1}{2}\Omega^2\frac{\partial^2}{\partial k_i^2} - E_{m,k_i}$ are the matrix elements of H_{qi} in the Bloch basis in the subspace of m. With this setup, we have $V_x = 0$, so for the x-component, equation (2.30) yields

$$n_x = k_x \tag{2.48}$$

$$\varepsilon_{m,n_x} = E_{m,k_x} \tag{2.49}$$

and naturally,

$$|\psi_{m,n_x}\rangle = |\Phi_{m,k_x}\rangle\,. \tag{2.50}$$

Therefore the quantum wire eigenfunctions for band m can be written as

$$|\psi_{m,n}\rangle = |\Phi_{m,\mathbf{k}_x}\rangle \otimes \left|\psi_{m,n_y}\right\rangle \otimes |\psi_{m,n_z}\rangle\,. \tag{2.51}$$

Field polarization along axis of wire

If we set the polarization of the field along the axis of the wire, $\hat{x}$, then the interaction Hamiltonian is only a function of x, so that

$$\mathbf{F}(t) = F_x(t)\hat{\mathbf{x}}, \tag{2.52}$$

$$\therefore H_{int} = \mathbf{r}\cdot\mathbf{F}(t) = F_x(t)x. \tag{2.53}$$

Now we can simplify the matrix elements of H_{int} as

$$\langle\psi_{m,n}|\, H_{int}\, |\psi_{m,n'}\rangle = F_x\,\langle\phi_{m,k_x}|\, x\, \left|\phi_{m,k_x'}\right\rangle \delta_{n_y,n_y'}\delta_{n_z,n_z'}. \tag{2.54}$$

Plugging this back into (2.37) and this time writing the band index as well, we get

$$i\dot{\beta}_{m,n} = \varepsilon_{m,n}\beta_{m,n} + F_x\sum_{m,k_x'}\langle\Phi_{m,k_x}|\, x\, \left|\Phi_{m,k_x'}\right\rangle \beta_{m,k_x',n_y,n_z}. \tag{2.55}$$

Here we note that $\beta_{m,n} = \beta_{m,k_x,n_y,n_z}$. Equation (2.55) is identical to the TDSE for bulk crystals (1.20) for a field polarized in $\hat{\mathbf{x}}$, but with eigenvalues $\varepsilon_{m,n}$ instead of $E_{m,\mathbf{k}}$ and quantum number n instead of wave vector $\mathbf{k}$. Thus we can solve solve for the probability amplitudes β the same way we would for bulk crystals. However, we would still need to recover the probability amplitudes β as functions of $\mathbf{k}$ in order to calculate the polarization and currents. This requires a transformation to the Bloch basis, as discussed in the following section.

2.5 Calculation of observables

The intraband current

When the field is parallel to the axis of the quantum wire, the intraband current is given by

$$\mathbf{j}_{ra}(t) = \sum_{m=c,v} \int_{BZ} \mathbf{v}_m(k_x) n_m(\mathbf{k}, t) d^3\mathbf{k} \tag{2.56}$$

where $n_m(\mathbf{k}, t) = |a_{m,\mathbf{k}}(t)|^2 = |\langle \Phi_{m,\mathbf{k}} | \Psi(t) \rangle|^2$, and $\mathbf{v}_m(k_x) = \frac{\partial}{\partial k_x} E_m(k_x)\hat{\mathbf{x}}$ is the band velocity in the $\hat{\mathbf{x}}$ direction. We only take the x-component because there will be a significant net current only in the direction of the field. In other directions, due to centro-symmetricity, the currents will average to zero. Thus we can write the current in each band as

$$\mathbf{j}_{m,ra}(t) = \int \mathbf{v}_m(k_x) \left[\int n_m(\mathbf{k}, t) dk_y dk_z \right] dk_x. \tag{2.57}$$

Under any transformation of basis, inner products are invariant. Therefore, the total **band population**,

$$\rho_m(t) = \int_{BZ} n_m(\mathbf{k}, t) d^3\mathbf{k} \tag{2.58}$$

remains invariant. With the field parallel to the axis of the wire, we can show that the term in [ ] in Eqn.(2.57)s must also be invariant. To do this we expand the wavefunction in the Bloch basis (suppressing band-index m for brevity):

$$|\Psi(t)\rangle = \sum_{k_x,k_y,k_z} a_{\mathbf{k}}(t) \, |\Phi_{k_x}\rangle \otimes \left|\Phi_{k_y}\right\rangle \otimes |\Phi_{k_z}\rangle. \tag{2.59}$$

In the quantum wire basis, this is

$$|\Psi(t)\rangle = \sum_{k_x,n_y,n_z} \beta_n(t) \, |\Phi_{k_x}\rangle \otimes \left|\psi_{n_y}\right\rangle \otimes |\psi_{n_z}\rangle. \tag{2.60}$$

Taking the projection on $\langle \Phi_{k_x}|$ gives

$$\sum_{k_y,k_z} a_{\mathbf{k}}(t) \left|\Phi_{k_y}\right\rangle \otimes |\Phi_{k_z}\rangle = \sum_{n_y,n_z} \beta_n(t) \left|\psi_{n_y}\right\rangle \otimes |\psi_{n_z}\rangle. \tag{2.61}$$

Taking the norm square of both sides yields

$$\sum_{k_y,k_z} |a_{\mathbf{k}}|^2 = \sum_{n_y,n_z} |\beta_n|^2, \tag{2.62}$$

$$\text{but} \qquad \sum_{k_y,k_z} |a_{\mathbf{k}}|^2 \equiv \int n_m(\mathbf{k}, t) dk_y dk_z \tag{2.63}$$

which is the term in the [ ] in equation (2.57), so the intraband current is invariant under

the unitary transformation from quantum wire to Bloch basis. Thus we need not invoke a transformation for the calculation of the intraband current.

The interband current

To calculate the polarization, we do need a transformation. Let $\mathbf{U}_m$ be the unitary transformation operator that transforms between Bloch and quantum wire eigenstates for a given band:

$$\mathbf{U}_m \left|\Phi_{m,\mathbf{k}}\right\rangle = \left|\psi_{m,\mathbf{k}}\right\rangle \quad ; \quad \mathbf{U}_m^\dagger \left|\psi_{m,\mathbf{k}}\right\rangle = \left|\Phi_{m,\mathbf{k}}\right\rangle \tag{2.64}$$

where it is understood that the wave vector $\mathbf{k}$ in the Bloch basis that corresponds to the quantum number n in the quantum wire basis. The matrix elements of $\mathbf{U}_m$ in the Bloch basis are

$$\left\langle \Phi_{m,k}\right| \mathbf{U}_m \left|\Phi_{m,k'}\right\rangle = \left\langle \Phi_{m,k}|\psi_{m,n'}\right\rangle = \alpha_{m,n'k}. \tag{2.65}$$

In the quantum wire basis,

$$\left\langle \psi_{m,n}\right| \mathbf{U}_m \left|\psi_{m,n'}\right\rangle = \left\langle \Phi_{m,k}|\psi_{m,n'}\right\rangle = \alpha_{m,n'k}. \tag{2.66}$$

The matrix representation of $\mathbf{U}$ is therefore the same in either basis. In terms of the Bloch basis amplitudes, the polarization is given by

$$\mathbf{p}(\mathbf{k},t) = \mathbf{d}(\mathbf{k}) a^*_{c,\mathbf{k}} a_{v,\mathbf{k}}. \tag{2.67}$$

The transformation from β to a can be calculated as follows:

$$\begin{aligned} a_{m,\mathbf{k}} &= \left\langle \Phi_{m,k}|\Psi(t)\right\rangle & (2.68)\\ &= \left\langle \psi_{m,n}\right| \mathbf{U}_m \left|\Psi(t)\right\rangle . & (2.69) \end{aligned}$$

What this means is that if we represent $\Psi(t)$ in the quantum wire basis as a column vector of $\beta_{m,n}$, which we can call $\Psi_{\beta,m}$, then we can recover the column vector of $a_{m,\mathbf{k}}$ which we designate $\Psi_{a,m}$, using the matrix multiplication

$$U_m \Psi_{\beta,m} = \Psi_{a,m}. \tag{2.70}$$

Finally, we can write the polarization array $\mathbf{p}_{a_m}(t)$ in terms of β and the dipole array $\mathbf{d}$:

$$\mathbf{p}_{a_m}(t) = \mathbf{d} \Psi^\dagger_{a,c} U^\dagger_c U_v \Psi_{a,v}. \tag{2.71}$$

Each element of the array, indexed by $\mathbf{k}$ is therefore

$$\mathbf{p}(\mathbf{k},t) = \mathbf{d}(\mathbf{k}) \sum_{n,n'} a^*_{c,\mathbf{k}} U^\dagger_{c,n,\mathbf{k}} U_{v,\mathbf{k},n'} a_{v,\mathbf{k}}. \tag{2.72}$$

Numerically, equation (2.72) is the major modification to the calculation of HHG in solids in order to incorporate quantum wires. We have shown that intraband current is simply the bulk intraband current with modified eigenvalues, but the interband term undergoes significant theoretical modifcation. With this we conclude the theory part of

this thesis. In the next part of this thesis, we shall define the parameters used in the simulation and discuss the results obtained.

Part II

Results and Discussion

Chapter 3

Numerical Solution of the Two Band Equations

In this chapter we present a numerical solution of Eqs.(2.55) for a model semiconductor similar to ZnO. While the theory developed in the previous chapter is valid for three-dimensions (3D), due to computing time constraints, we will use a two-dimensional (2D) model. Though the 2D results will differ quantitatively from the 3D calculations, qualitatively the conclusions remain valid.

Two dimensional semiconductor model

The band structure for our 2D model semiconductor (in the absence of the quantum wire confining potential) is written as the sum of the bands along each individual axis in the same manner as presented in the previous chapter, i.e,

$$E_m(\mathbf{k}) = E_{m,x}(k_x) + E_{m,y}(k_y) \tag{3.1}$$

where $m = c, v$. Each of the individual 1D bands can be expressed in terms of Fourier components as,

$$E_{v,i}(k_i) = \sum_{j=0}^{\infty} C_{v,i}^{j} \cos(jk_i a_i) \tag{3.2}$$

$$E_{c,i}(k_i) = E_g + \sum_{j=0}^{\infty} C_{c,i}^{j} \cos(jk_i a_i) \tag{3.3}$$

where $i = x, y$ and $(a_x, a_y) = (5.32, 9.83)$ are the lattice constants given in atomic units; our minimum bandgap is $E_g = 0.01213$ a.u. (3.3 eV). The values for C are given in Table 3.1. For the band structure along the x-direction we use the band along Γ-M given in Ref. [40]; this is the direction along which our laser field will be directed. For the y-direction we use a structure similar to Γ-A given in Ref. [40]; however, here we have set the bandwidths of the valence and conduction bands to be equal for simplicity.

A quantity of particular interest is the band gap, $\Delta E(k)$, the difference between the conduction band and valence band. The maximum photon energy that an interband transition can emit is the maximum bandgap energy in the direction of the field [28, 41],

given by

$$\omega_{max} = \max[\Delta E(k)] \tag{3.4}$$

where ω_{max} is the angular frequency of such a photon.

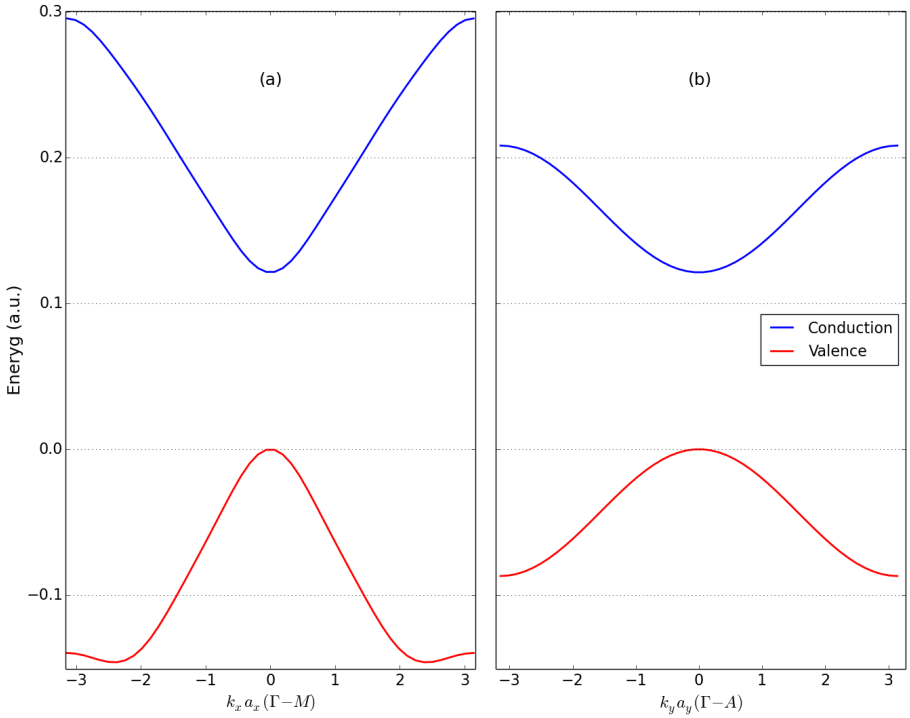

Figure 3.1: Band structure for the bulk solid depicting conduction and valence band energy as a function of ka in the (a) Γ-M direction, and (b) Γ-A direction.

Coefficients	Valence Band ($m = v$)	Conduction Band ($m = c$)
$C^0_{m,x}$	-0.0928	0.0898
$C^1_{m,x}$	0.0705	-0.0814
$C^2_{m,x}$	0.0200	-0.0024
$C^3_{m,x}$	-0.0012	-0.0048
$C^4_{m,x}$	0.0029	-0.0003
$C^5_{m,x}$	0.0006	-0.0009
$C^0_{m,y}$	-0.0435	0.0435
$C^1_{m,y}$	0.0435	-0.0435

Table 3.1: Fourier coefficients of the band according to Ref. [40], with two key differences - we have omitted the Γ-K direction and made the conduction band coefficients equal in magnitude to the valence band coefficients.

As already noted, we have set the valence band coefficients to be of the same magnitude as the conduction band coefficients in the y direction. By doing so, the unitary

operator for both valence and conduction bands (Sec.2.5), will be identical, i.e,

$$U_c = U_v. \tag{3.5}$$

For this to be true, the x-direction bands need not be equal since there is no confinement in that direction. Thus the polarization given by

$$\mathbf{p}_{a_m}(t) = \mathbf{d}\Psi^{\dagger}_{a,c}U^{\dagger}_c U_c \Psi_{a,v} \tag{3.6}$$

would be invariant under transformation because U_c is a unitary operator with the property

$$U^{\dagger}_c U_c = I, \tag{3.7}$$

where I is the identity operator. This reduces the transformation time dramatically, and due to time constraints, we chose this setup.

Potential and width of wire

In 2D we apply a confining potential in the y direction (Γ-A) only, so

$$V(y) = \frac{1}{2}\Omega^2 y^2 \tag{3.8}$$

The 'width', D is defined as the width of the ground state wavefunction of a harmonic oscillator, i.e,

$$D = \sqrt{\frac{1}{\Omega}} \tag{3.9}$$

In our simulations we vary D in order to study the effect of confinement on the harmonic spectrum.

Solving the eigenvalue equations

To calculate the eigenvalues and vectors, we represent the operator defined in Eqn.(2.47),

$$\Gamma_{m,k_y} = \frac{1}{2}\Omega^2 \frac{\partial^2}{\partial k_y^2} - E_{m,k_y}, \tag{3.10}$$

in a discretized matrix form. We then numerically calculate the eigenvalues of this matrix. To do this, we first discretize k_i into N_i equally spaced points in the first Brillouin zone, for $i = x, y$. The spacing between the points is then

$$\Delta k_i = \frac{K_i}{N_i} \tag{3.11}$$

where K_i is the length of the Brillouin zone in the i^{th} direction. Centering the Brilloiun zone around the Γ-point ($\mathbf{k} = 0$), the wave numbers k_i are in the discrete interval

$$-\frac{K_i}{2} \leq k_i < \frac{K_i}{2} \tag{3.12}$$

with a spacing of Δk_i. With this we discretize a continuous function $f(k)$ as f_j, where

$$f_j = f(-\tfrac{1}{2}K_i + j\Delta k_i) \tag{3.13}$$

where j is an integer ranging from 0 to $N_i - 1$. With this definition, in Eqn.(3.10),we write the bulk band term (E_{m,k_y}) as a diagonal matrix $\mathbf{E}_m$ with diagonal elements

$$\mathbf{E}_m^{jj} = E_{m,j} \tag{3.14}$$

where the superscripts represent the row and column index. Next we approximate the action of the differential operator $\partial^2 f(k)/\partial k^2$ on a function $f(k)$ in this k-grid using the 5-point-stencil [42],

$$\frac{\partial^2 f(k)}{\partial k^2} \approx \frac{-f_{j-2} + 16f_{j-1} - 30f_j + 16f_{j+1} - f_{j+2}}{12(\Delta k)^2} \tag{3.15}$$

Thus, if we assume f to be periodic in the Brillouin zone, then we can write the harmonic oscillator operator, $\frac{1}{2}\Omega^2\frac{\partial^2}{\partial k^2}$ as

$$\mathbf{M} = \frac{\Omega^2}{24\Delta k^2}\begin{bmatrix} -30 & 16 & -1 & 0 & \dots & \dots & 0 & -1 & 16 \\ 16 & -30 & 16 & -1 & 0 & \dots & \dots & 0 & -1 \\ -1 & 16 & -30 & 16 & -1 & 0 & \dots & \dots & 0 \\ 0 & -1 & 16 & -30 & 16 & -1 & 0 & & \vdots \\ \vdots & \ddots & \ddots & \ddots & \ddots & \ddots & \ddots & \ddots & \vdots \\ \vdots & & 0 & -1 & 16 & -30 & 16 & -1 & 0 \\ 0 & \dots & \dots & 0 & -1 & 16 & -30 & 16 & -1 \\ -1 & 0 & \dots & \dots & 0 & -1 & 16 & -30 & 16 \\ 16 & -1 & 0 & \dots & \dots & 0 & -1 & 16 & -30 \end{bmatrix}$$

where the periodic conditions are met by including the terms in the off-diagonal corners. Thus the total discrete matrix operator for Γ is an N_y by N_y matrix,

$$\mathbf{W} = \mathbf{M} + \mathbf{E}_m. \tag{3.16}$$

By numerically calculating the eigenvalues (shown in Fig.(3.2)) and vectors of $\mathbf{W}$, we retrieve the discretized eigenfunctions

$$\alpha_{m,n_y,j} = \alpha_{m,n_y}(-\tfrac{1}{2}K_y + j\Delta k_y) \tag{3.17}$$

and their corresponding eigenvalues ε_{m,n_y}, where j and n_y are integers in the range $[0 \dots N_y - 1]$. In our calculations, we use $N_x = 600$ points along Γ-M, and $N_y = 2000$ points along Γ-A. In the lateral (Γ-A) direction, the number of points we take is the number of eigenstates we take into account. As there is no upper limit to this number, we chose it so that the range of eigenvalues, $\varepsilon_{N_y} - \varepsilon_0$, covers at least the bandwidth of the conduction band plus the band gap. In the bulk case, any state near the top of the

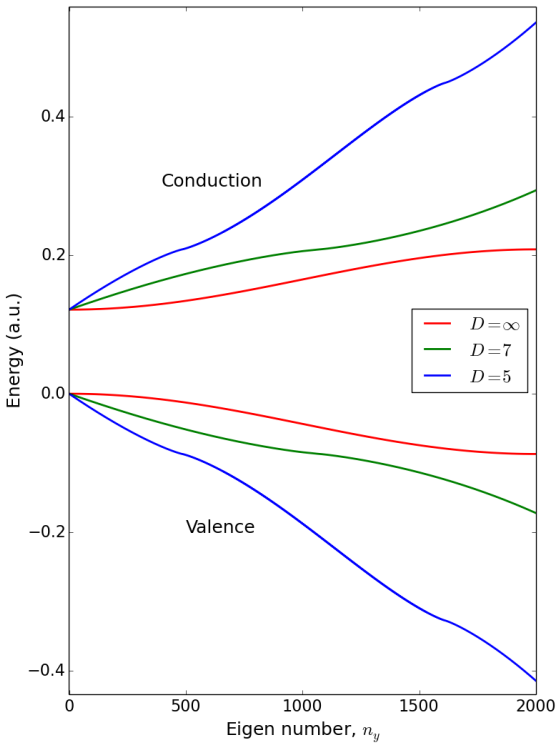

Figure 3.2: Here we present the quantum wire eigenvalues, ε_{m,n_y} for both bands in the y-direction (Γ-A) as a function of the corresponding quantum number, n_y, for three different widths, 5nm, 7nm and bulk. The eigenvalues for the bulk crystal(red) correspond to $E_{m,y}(k_y)$ when plotted in the Brilluoin zone. As the width is decreased, the minimum band-gap at $n_y = 0$ increases due to increase in zero-point energy, but this is negligible compared to the band-gap and is not visible in this plot. However, as the width is decreased from bulk to 7nm (green), both the conduction and valence curves get steeper, with higher bandgaps at higher eigen numbers, n_y. For the 5nm, the bandgap is even steeper than the 7nm. The narrower the width of the quantum wire, the steeper the rise in bandgap in the lateral directions.

conduction band is extremely unlikely to be occupied for the field strengths we explore. Thus, in quantum wires any state with ε_n higher than the peak conduction band energy has negligible probability of occupation. In the Γ-M direction, the eigenvalues will be the bulk band structure which we know analytically from Eqn.(3.3), thus we are simply dividing the whole energy spectrum in the Brillouin zone into $N_x = 600$ points.

Driving field

In order to investigate HHG, the system is exposed to an intense mid-infrared laser pulse linearly polarised in $\hat{\mathbf{x}}$. The field has a vector potential of the form $\mathbf{A}(t) = A_x(t)\hat{\mathbf{x}}$, where

$$A_x(t) = \frac{F_0}{\omega} \exp\left[-\frac{(t-t_c)^2}{(\sigma\tau)^2}\right] \cos(\omega t) \tag{3.18}$$

with τ the total duration of the simulation; σ is the pulse width parameter and is equal to 0.1 for all calculations; $t_c = \tau/2$ is the peak time of the pulse and ω is the angular laser pulse frequency. Here we used a typical mid-infrared wavelength, $\lambda = 3.25\mu$m for all simulations. The maximum field strenght, F_0 is varied to study the effects of different laser intensities on the harmonic spectrum. Finally, the laser electric field can be determined from

$$F_x(t) = -\frac{dA_x(t)}{dt}. \tag{3.19}$$

These laser parameters will be used throughout the rest of the thesis.

Simulation Results

Using our newly obtained band structure, we solve Eqns.(2.55) in the presence of a mid-IR laser field of wavelength of 3.25 μm. To do this Eqs.(2.55) are integrated in time using a fourth-order Runge-Kutta method [43]. The Gaussian-modulated pulse (as described by Eqns.(3.18) and (3.19)) has a FWHM of 10 cycles, and is propagated for a time window of 20 cycles. As mentioned before, along the field direction we use 600 grid points to represent the bulk band structure in Γ-M; and 2000 grid points along Γ-A. Here we have 600 $\times$ 2000 individual 1D differential equations to solve. A calculation of this size takes approximately 4 hours to complete. Fig.(3.3) compares the harmonic spectrums

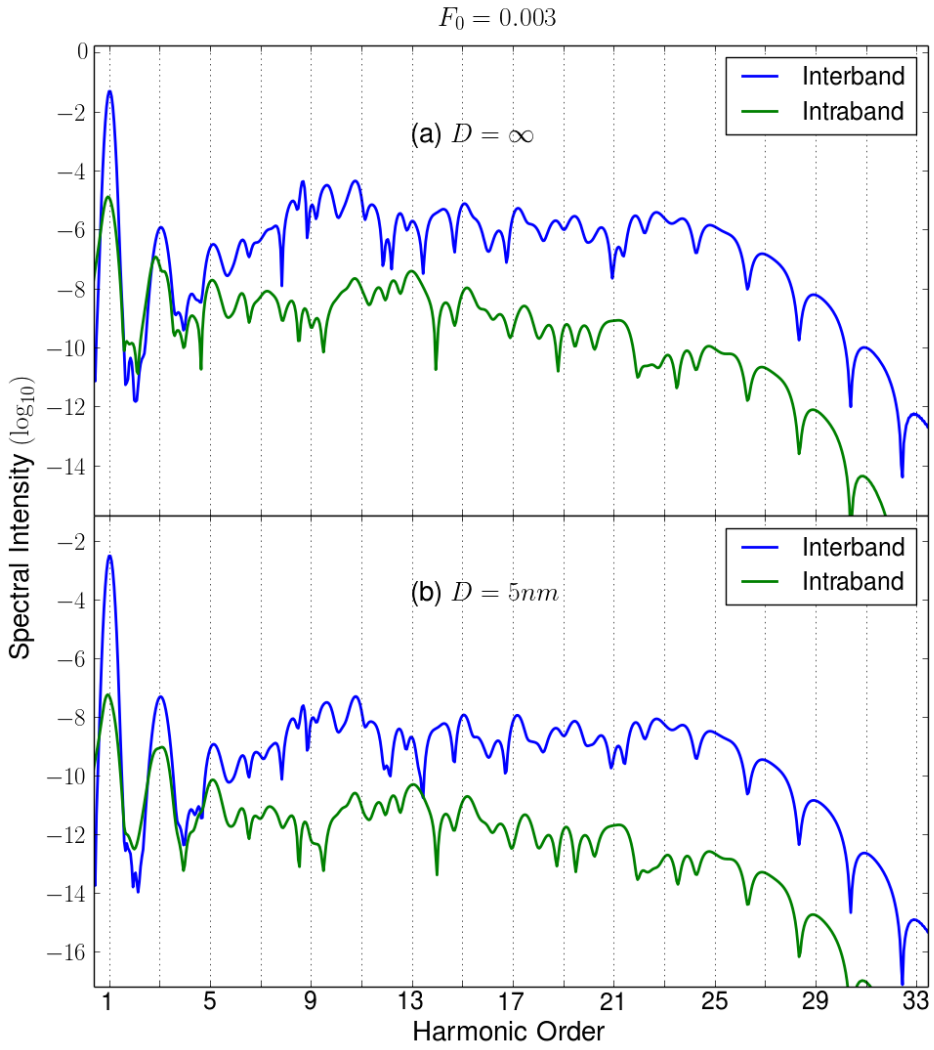

Figure 3.3: (a) Bulk inter and intraband spectrums. (b) Spectrums for a $5nm$ quantum wire.

generated by the inter and intraband currents for the bulk crystal (Fig.3.3(a)) and a 5 nm quantum wire (Fig.3.3(b)) for a peak field strength of 0.003 a.u. In both cases the interband dominates over the intraband, which is consistent with theoretical predictions [28–30, 44] and experimental observation [22] for HHG in semiconductor crystals exposed to intense mid-IR fields. The key difference between Fig.3.3(a) and Fig.3.3(b) is that the harmonics are suppressed for the quantum wire which is shown in more detail in Fig.(3.4).

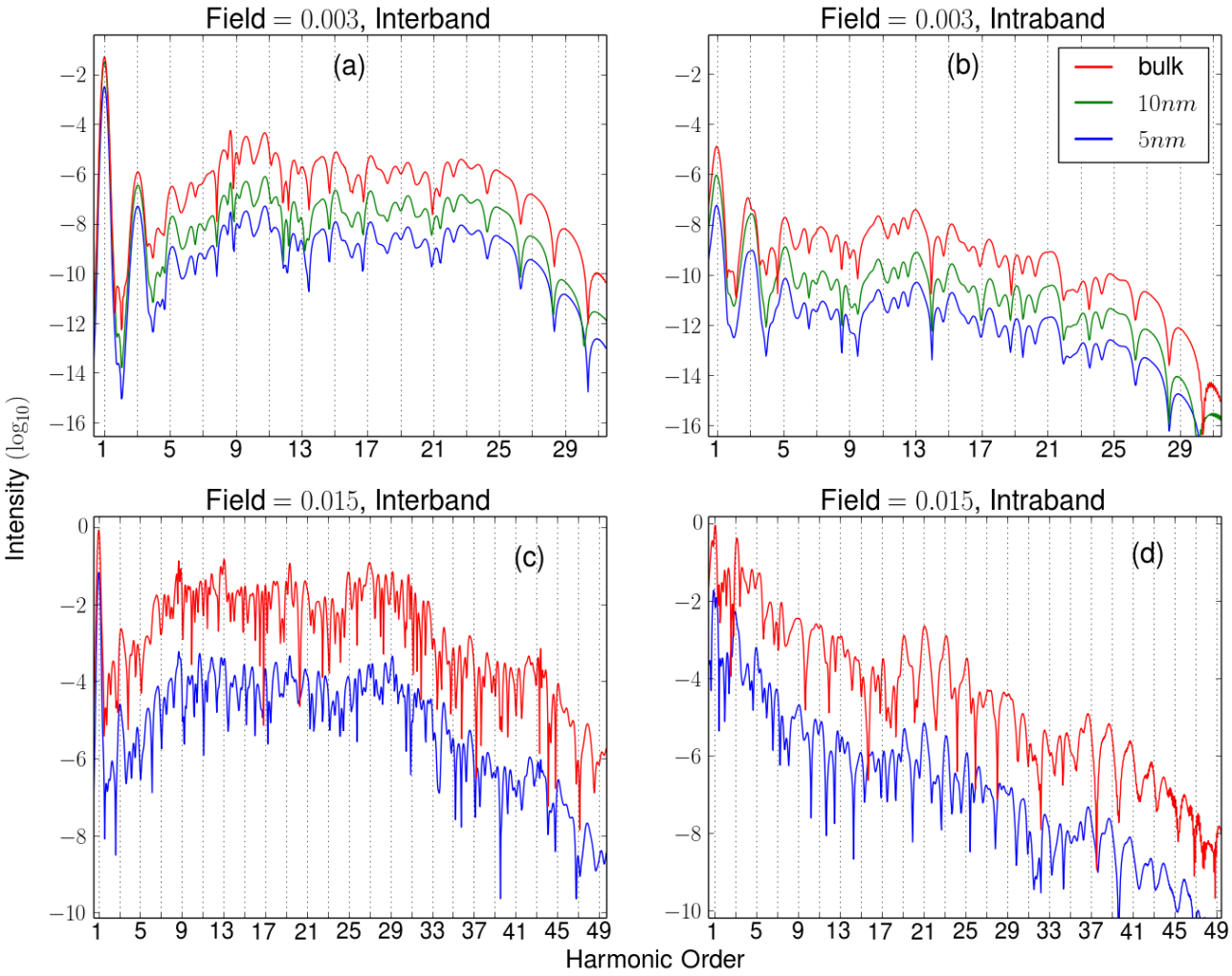

Figure 3.4: HHG of different widths compared. Plots (a) and (b) are the interband and intraband spectrums respectively, at a field strength of $F_0 = 0.003$ a.u. Similarly, plots (c) and (d) are for a field strength of $F_0 = 0.015$ a.u. Plots (a) and (b) depict the spectrums for a bulk crystal(red), 10nm wire(green) and 5nm wire(blue). The 10nm spectrums have been omitted in plots (c) and (d) for the sake of clarity.

Figure 3.4 illustrates the influence of the quantum wire width on the behaviour of interband and intraband harmonic spectrums for a low and high field strength. For both the inter and intraband spectrums of the quantum wires the harmonics are suppressed with respect to the bulk crystal. To see if this behaviour persists at high field strengths, plots (a) and (b) of Fig.(3.4) are repeated in (c) and (d) for a field strength of $F_0 = 0.015$ a.u. As with the lower field strength, the harmonics spectrums from both interband and intraband contributions are suppressed relative to the bulk crystal.

In order to investigate the reason for the suppression of harmonics we look at the final ionization (population in the conduction band at the end of the pulse) as a function of wire width. Fig.(3.5) shows the final conduction band population vs wire width for several field strengths. For all field strengths a clear trend emerges: as the width of the quantum wire is decreased, so to is the final conduction band population. This drop in ionization with wire width is in line with the decrease in harmonic intensity. This make

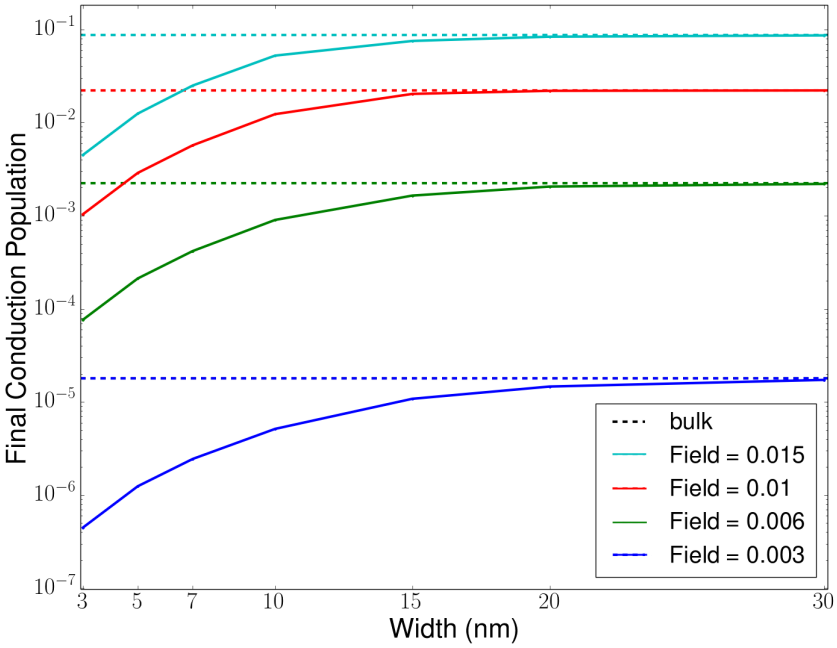

Figure 3.5: Final conduction population vs. width for different field strengths. Each of the solid curves represents a different peak field strength and the dashed line with the corresponding colour indicates the final ionisation for the bulk crystal at the same field strength.

sense because as the width of the wire is decreased, the eigenvalues spectrum for it's valence and conduction bands in the lateral direction become steeper (see Fig. 3.2). This results in less population transfer due to the steeper increase in bandgap away from the band minimum.

This suppression of ionization has an important consequence. One of the challenges of strong field physics in solid state systems is that the material under study can become damaged if the field strength is too high. This limits investigation of processes in solids to field strengths below the damage threshold. These results indicate that it may be possible to use an array of quantum wires to increase the damage threshold.

For a possible benefit of increasing the damage threshold, we look back at Fig.(3.3). Here the harmonic spectrum has an extended plateau region followed by an exponential drop off of the harmonic intensity. The last harmonic before the exponential drop is known as the cutoff harmonic. These features can also be seen in harmonic plots of Fig.(3.4). Increasing the damage threshold brings the possibility of extending the maximum harmonic order without damaging the material.

While the maximum cutoff harmonic for the interband spectrum is limited by the maximum bandgap at the Brillouin zone edge [28,41], the intraband cutoff does not have such a restriction. Figure 3.6 shows the cutoff as a function of the peak field strength for both the interband and intraband spectrums for a 5 nm quantum wire. The interband cutoff behaves as expected and saturates at the 31st harmonic corresponding to the maximum energy bandgap (Eqn.(3.4)). By contrast, the cutoff of the intraband spec-

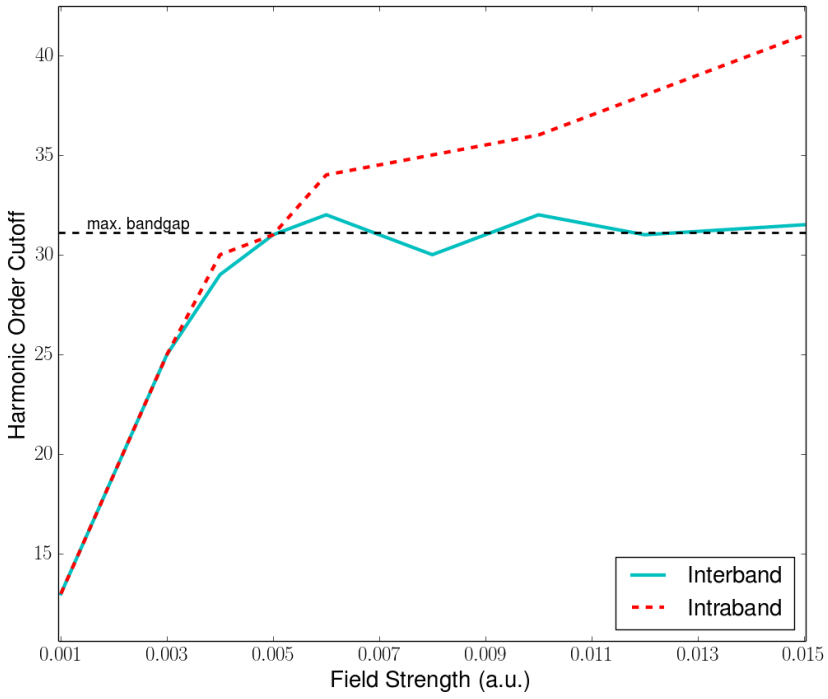

Figure 3.6: Harmonic cutoff vs. field strength for a 5nm quantum wire

trum continues to rise with the field strength, rising to the 41st harmonic at $F_0 = 0.015$ a.u., where the final ionization is just above 1%. While interband harmonics are the dominant mechanism for laser wavelengths in the mid-IR range, intraband harmonics are the dominant mechanism for THz pulses [20]. As such, this result may prove important for researches involving THz fields, particularly in the study of THz driven accelerators which could greatly impact the development of X-ray science and medical therapy with X-rays [38].

Conclusion

We have extended the two-band theoretical framework for HHG in bulk solids to include confined quantum systems such as quantum wells, wires and dots.The resultant equations are valid for a general confinement and can be easily implemented when the field is directed along an unconfined direction. For fields directed along a confined direction, the transformation procedure in Chapter 2 needs to be modified.

In the second part, we investigated HHG for two-dimensional quantum wires of various widths confined in the direction perpendicular to a mid-IR driving field by a simple harmonic potential. The results confirm that at all the field strengths explored with a mid-infra red driving field, the interband harmonics dominate over the intraband beyond the minimum band gap harmonic. Furthermore, decreasing the width had the effect of suppressing the total intensity of the harmonic spectrums. This correlates with the fact that the band structure for narrower wires have a steeper increase in band gap away

from the band minimum. This has the desired effect of reducing the final ionisation for a given field strength, thus allowing us to explore higher field strengths without material damage. Higher field strengths increase the harmonic cutoff, but only upto a point for the interband spectrum, whose harmonics are limited by the maximum bandgap. However, there is no such limit for the intraband. Since we are able to explore higher field strengths with quantum wires than with bulk crystals, we may be able to study a range of field strengths in which the intraband currents yield much higher harmonics than the interband. This could be especially interesting with the use of terahertz driving fields that can generate harmonics of much higher order.

The theory developed in this thesis has opened a pathway for the exploration of nano-confinement on HHG in solid state systems, and the results provide a motivation for exploring this avenue of research. As already mentioned, the theory could be easily applied to quantum wells, or three dimensional quantum wires. It could also serve as a starting point for dealing with quantum dots. In addition, we demonstrated that we can control the damage threshold of a material by altering the dimensions of the wire. This has important implications for the development of all-solid state linear accelerators, which has potential applications for new areas of research such as ultrafast electron diffraction and X-ray science [38]. In a broader sense, we have provided some new motivation for the nano-engineering of strong field solid state physics.

Appendix A

Effective Mass Approximation

If the harmonic oscillator frequency, Ω is high enough to confine the electron near the Γ point, we can expand the band structure around $\mathbf{k} = 0$ in a Taylor series upto the second order, giving us the effective mass approximation :

$$E_m(\mathbf{k}) = E_m(0) + \frac{1}{2}\sum_{i,j}\frac{\partial^2 E_m}{\partial k_i k_j}(0)k_i k_j + O(\mathbf{k}^3) \tag{A.1}$$

where $i, j = x, y, z$. The bulk band is taken to be separable, in accordance with Ref. [40]. So

$$E_m(\mathbf{k}) = E_{m,x}(k_x) + E_{m,y}(k_y) + E_{m,z}(k_z), \tag{A.2}$$

$$\therefore \frac{\partial^2 E_m}{\partial k_i k_j}k_i k_j = \frac{\partial^2 E_{m,i}}{\partial k_i^2}k_i^2\delta_{i,j} \tag{A.3}$$

and so,

$$E_m(\mathbf{k}) = E_m(0) + \frac{1}{2}\sum_{i}\frac{\partial^2 E_{m,i}}{\partial k_i^2}(0)k_i^2. \tag{A.4}$$

Near the Γ point, we use the Fourier expansion using only the first two coefficients (see Table 3.1),

$$E_{m,i}(k_i) = \Delta_{m,i}(1 - \cos k_i a_i) + E_g\delta_{m,c} \tag{A.5}$$

where $\Delta_{m,i}$ and $-\Delta_{m,i}$ are the first two Fourier coefficients in the mth band and ith direction. This gives us

$$\frac{\partial^2 E_{m,i}}{\partial k_i^2}(0)k_i^2 = \Delta_{m,i}k_i^2 a_i^2 \quad \text{and} \quad E_m(0) = 0 \tag{A.6}$$

$$\therefore E_m(\mathbf{k}) = \frac{1}{2}\sum_i \Delta_{m,i}k_i^2 a_i^2 + E_g\delta_{m,c} \tag{A.7}$$

or for the ith component,

$$E_m(k_i) = \frac{1}{2}\Delta_{m,i}k_i^2 a_i^2 + \frac{1}{3}E_g\delta_{m,c} \tag{A.8}$$

Next, we insert this back into Eqn.2.45 and obtain

$$(\varepsilon_{m,n_i} - \frac{1}{3}E_g\delta_{m,c})\alpha_{m,n_i,k_y} = \alpha_{m,n_i,k_i}\frac{1}{2}\Delta_{m,i}k_i^2a_i^2 - \frac{1}{2}\Omega^2\frac{\partial^2}{\partial k_i^2}\alpha_{m,n_i,k_i} \tag{A.9}$$

Eqn.(A.9) has known analytical solutions, the harmonic oscillator eigenfunctions. This approximation can be used to simplify the calculation of eigenvalues and eigenvectors, and perhaps explore analytical approaches to HHG in confined quantum systems.

Appendix B

The $\mathbf{k} \cdot \mathbf{p}$ Theory

In this Appendix we use the following notation for the periodic part of Bloch functions, $u_{\lambda,k}$

$$|u_{\lambda,\mathbf{k}}\rangle = |\lambda, \mathbf{k}\rangle \tag{B.1}$$

where λ is the band index. In the $\mathbf{k} \cdot \mathbf{p}$ approximation [32], $|\lambda, \mathbf{k}\rangle$ is expanded around the Γ point and first order peturbation theory applied to give

$$|\lambda, \mathbf{k}\rangle = |\lambda\rangle + \sum_{\eta \neq \lambda} \frac{|\eta\rangle \, \mathbf{k} \cdot \langle \eta | \, \mathbf{p} \, | \lambda \rangle}{E_\lambda(0) - E_\eta(0)} \tag{B.2}$$

Taking the projection of $|\lambda, \mathbf{k}\rangle$ on the $\mathbf{r}$ basis yields

$$\langle \mathbf{r} | \lambda, \mathbf{k} \rangle = u_{\lambda,\mathbf{k}}(\mathbf{r}) = u_{\lambda,0}(\mathbf{r}) + \sum_{\eta \neq \lambda} \frac{u_{\eta,0}(\mathbf{r}) \mathbf{k} \cdot \langle \eta | \, \mathbf{p} \, | \lambda \rangle}{E_\lambda(0) - E_\eta(0)} \tag{B.3}$$

In writing the full Bloch wavefunction, the second term is often neglected for small $\mathbf{k}$:

$$\Phi_{m,\mathbf{k}} \approx u_{m,0} e^{im\Delta\mathbf{k}}. \tag{B.4}$$

In general, because of the periodicity of $u_{m,\mathbf{k}}$, any reciprocal lattice vector may be used instead of the Γ point, so

$$\Phi_{m,\mathbf{k}} \approx u_{m,\mathbf{K}} e^{im\mathbf{K}} e^{im\Delta\mathbf{k}}. \tag{B.5}$$

which is what is used in Eqn.(2.11).

Dipole moment calculation

In order to show that

$$\mathbf{d}_{\lambda,\lambda}(\mathbf{k}) = i \int_{L^3} u^*_{\lambda,\mathbf{k}} \nabla_{\mathbf{k}'} u_{\lambda,\mathbf{k}'} d^3 r = 0 \tag{B.6}$$

$$\tag{B.7}$$

we insert Eqn.(B.3) above. The differential factor in the integrand will equate to

$$\nabla_{\mathbf{k}} u_{\lambda,\mathbf{k}}(\mathbf{r}) = \sum_{\eta \neq \lambda} \frac{u_{\eta,0}(\mathbf{r}) \langle \eta | \mathbf{p} | \lambda \rangle}{E_\lambda(0) - E_\eta(0)} \tag{B.8}$$

In the two band model, ($\lambda = c, v$ and $\eta = v, c$) this reduces to

$$\nabla_{\mathbf{k}} u_{\lambda,\mathbf{k}}(\mathbf{r}) = \frac{1}{E_g} u_{\eta,0}(\mathbf{r}) \langle \eta | \mathbf{p} | \lambda \rangle \tag{B.9}$$

where $E_\lambda(0) - E_\eta(0)$ is the minimum bandgap. Therefore,

$$\int_{L^3} u^*_{\lambda,\mathbf{k}} \nabla_{\mathbf{k}'} u_{\lambda,\mathbf{k}'} d^3r \tag{B.10}$$

$$= \frac{1}{E_g} \int_{L^3} \left\{ u^*_{\lambda,0} + u^*_{\eta,0}(\mathbf{r}) \mathbf{k} \cdot \langle \lambda | \mathbf{p}^\dagger | \eta \rangle / E_g \right\} u_{\eta,0}(\mathbf{r}) \langle \eta | \mathbf{p} | \lambda \rangle d^3r \tag{B.11}$$

$$= \frac{\mathbf{p}_{\eta\lambda}}{E_g} \cancelto{0}{\int_{L^3} u^*_{\lambda,0} u_{\eta,0}(\mathbf{r})^* d^3r} + \frac{(\mathbf{k} \cdot \mathbf{p}^\dagger_{\lambda,\eta}) \mathbf{p}_{\eta,\lambda}}{E_g^2} \int_{L^3} u^*_{\eta,0} u_{\eta,0}(\mathbf{r}) d^3r \tag{B.12}$$

$$= \frac{(\mathbf{k} \cdot \mathbf{p}^\dagger_{\lambda,\eta}) \mathbf{p}_{\eta,\lambda}}{E_g^2} \tag{B.13}$$

where we have used Bloch orthonormality to evalute the integrals; and $\mathbf{p}_{\eta,\lambda} = \langle \eta | \mathbf{p}^\dagger | \lambda \rangle$. In our analysis, we neglect the term $\frac{(\mathbf{k} \cdot \mathbf{p}^\dagger_{\lambda,\eta}) \mathbf{p}_{\eta,\lambda}}{E_g^2}$ for small $\mathbf{k}$. Similarly, it can be shown that

$$\mathbf{d}_{\lambda,\eta}(\mathbf{k}) = \int_{L^3} u^*_{\eta,\mathbf{k}} \nabla_{\mathbf{k}'} u_{\lambda,\mathbf{k}'} d^3r = \frac{\mathbf{p}_{\eta\lambda}}{E_g} \tag{B.14}$$

when $\eta \neq \lambda$, which is in accordance with Ref. [29].

References

[1] Robert W. Boyd. Chapter 1 - the nonlinear optical susceptibility. In Robert W. Boyd, editor, *Nonlinear Optics (Third Edition)*, pages 1 – 67. Academic Press, Burlington, third edition edition, 2008.

[2] P. B. Corkum. Plasma perspective on strong field multiphoton ionization. *Phys. Rev. Lett.*, 71:1994–1997, Sep 1993.

[3] M. Lewenstein, Ph. Balcou, M. Yu Ivanov, Anne L'huillier, and Paul B Corkum. Theory of high-harmonic generation by low-frequency laser fields. *Physical Review A*, 49(3):2117, 1994.

[4] P. B. Corkum and F. Krauz. Attosecond science. *Nat. Phys.*, 3:381, Sep 2007.

[5] Thomas Brabec and Ferenc Krausz. Intense few-cycle laser fields: Frontiers of nonlinear optics. *Rev. Mod. Phys.*, 72:545–591, Apr 2000.

[6] P. Agostini and L. F. DiMauro. The physics of attosecond light pulses. *Rep. Prog. Phys.*, 67:813, 2004.

[7] S. Patchkovskii N. Dudovich D. Villeneuve P. B. Corkum M. Yu. Ivanov O. Smirnova, Y. Mairesse. High harmonic interferometry of multi-electron dynamics in molecules. *Nature*, 460:972, 2009.

[8] H. J. Wörner, J. B. Bertrand, D. V. Kartashov, P. B. Corkum, and D. M. Villeneuve. Following a chemical reation using high-harmonic interferometry. *Nature*, 466:604, 2010.

[9] H. J. Wörner, J. B. Bertrand, P. B. Corkum, and D. M. Villeneuve. High-harmonic homodyne detection of the ultrafast dissociation of Br_2 molecules. *Phys. Rev. Lett.*, 105:103002, Sep 2010.

[10] Anh-Thu Le, R. R. Lucchese, S. Tonzani, T. Morishita, and C. D. Lin. Quantitative rescattering theory for high-order harmonic generation from molecules. *Phys. Rev. A*, 80:013401, Jul 2009.

[11] Jiro Itatani, Jérôme Levesque, Dirk Zeidler, Hiromichi Niikura, Henri Pépin, Jean-Claude Kieffer, Paul B Corkum, and David M Villeneuve. Tomographic imaging of molecular orbitals. *Nature*, 432(7019):867–871, 2004.

[12] S. Baker *et al.* Probing proton dynamics in molecules on an attosecond time scale. *Science*, 312:424, 2006.

[13] N. H. Burnett, H. A. Baldis, M. C. Richardson, and G. D. Enright. Harmonic generation in CO_2 laser target interaction. *Applied Physics Letters*, 31:172–174, August 1977.

[14] A. McPherson, G. Gibson, H. Jara, U. Johann, and T. S. Luk. Studies of multiphoton production of vacuum-ultraviolet radiation in the rare gases. *Journal of the Optical Society of America B Optical Physics*, 4:595–601, April 1987.

[15] X. F. Li, A. L'Huillier, M. Ferray, L. A. Lompré, and G. Mainfray. Multiple-harmonic generation in rare gases at high laser intensity. *Phys. Rev. A*, 39:5751–5761, Jun 1989.

[16] J. W. G. Tisch, R. A. Smith, J. E. Muffett, M. Ciarrocca, J. P. Marangos, and M. H. R. Hutchinson. Angularly resolved high-order harmonic generation in helium. *Phys. Rev. A*, 49:R28–R31, Jan 1994.

[17] R. Santra and A. Gordon. Three-step model for high-harmonic generation in many-electron systems. *Phys. Rev. Lett.*, 96:073906, Feb 2006.

[18] R. Loudon. *The Quantum Theory of Light*. OUP Oxford, 2000.

[19] Shambhu Ghimire, Anthony D DiChiara, Emily Sistrunk, Pierre Agostini, Louis F DiMauro, and David A Reis. Observation of high-order harmonic generation in a bulk crystal. *Nature physics*, 7(2):138–141, 2011.

[20] Olaf Schubert, Matthias Hohenleutner, Fabian Langer, Benedikt Urbanek, C. Lange, U. Huttner, D. Golde, T. Meier, M. Kira, Stephan W. Koch, et al. Sub-cycle control of terahertz high-harmonic generation by dynamical Bloch oscillations. *Nature Photonics*, 8(2):119–123, 2014.

[21] B Zaks, RB Liu, and MS Sherwin. Experimental observation of electron-hole recollisions. *Nature*, 483(7391):580–583, 2012.

[22] G Vampa, TJ Hammond, N Thiré, BE Schmidt, F Légaré, CR McDonald, T Brabec, and PB Corkum. Linking high harmonics from gases and solids. *Nature*, 522(7557):462–464, 2015.

[23] Shambhu Ghimire, Anthony D. DiChiara, Emily Sistrunk, Urszula B. Szafruga, Pierre Agostini, Louis F. DiMauro, and David A. Reis. Redshift in the optical absorption of ZnO single crystals in the presence of an intense midinfrared laser field. *Phys. Rev. Lett.*, 107:167407, Oct 2011.

[24] Tran Trung Luu, M Garg, S Yu Kruchinin, Antoine Moulet, M Th Hassan, and Eleftherios Goulielmakis. Extreme ultraviolet high-harmonic spectroscopy of solids. *Nature*, 521(7553):498–502, 2015.

[25] Shambhu Ghimire, Anthony D. DiChiara, Emily Sistrunk, Georges Ndabashimiye, Urszula B. Szafruga, Anis Mohammad, Pierre Agostini, Louis F. DiMauro, and David A. Reis. Generation and propagation of high-order harmonics in crystals. *Phys. Rev. A*, 85:043836, Apr 2012.

[26] Peter G. Hawkins and Misha Yu. Ivanov. Role of subcycle transition dynamics in high-order-harmonic generation in periodic structures. *Phys. Rev. A*, 87:063842, Jun 2013.

[27] A F Kemper, B Moritz, J K Freericks, and T P Devereaux. Theoretical description of high-order harmonic generation in solids. *New Journal of Physics*, 15(2):023003, 2013.

[28] G Vampa, CR McDonald, G Orlando, PB Corkum, and T Brabec. Semiclassical analysis of high harmonic generation in bulk crystals. *Physical Review B*, 91(6):064302, 2015.

[29] G Vampa, CR McDonald, G Orlando, DD Klug, PB Corkum, and T Brabec. Theoretical analysis of high-harmonic generation in solids. *Physical review letters*, 113(7):073901, 2014.

[30] CR McDonald, G Vampa, PB Corkum, and T Brabec. Interband bloch oscillation mechanism for high-harmonic generation in semiconductor crystals. *Physical Review A*, 92(3):033845, 2015.

[31] Ashcroft N.W. and Mermin N.D. *Solid State Physics*. Hartcourt College, 1976.

[32] Haug H. and Koch S.W. *Quantum Theory of the Optical and Electronic Properties of Semiconductors*. World Scientific, 4th edition, 2004.

[33] P. Harrison. *Quantum Wells, Wires and Dots: Theoretical and Computational Physics of Semiconductor Nanostructures*. Wiley, 2005.

[34] T. D. Ladd, F. Jelezko, R. Laflamme, Y. Nakamura, C. Monroe, and J. L. O Brien. Quantum computers. *Nature*, 464:45–53, March 2010.

[35] R. C. Ashoori. Electrons in artificial atoms. *Nature*, 46:413, Feb 1996.

[36] Samuel W Eaton, Anthony Fu, Andrew B Wong, Cun-Zheng Ning, and Peidong Yang. Semiconductor nanowire lasers. *Nature Reviews Materials*, page 16028, 2016.

[37] D Golde, T Meier, and SW Koch. High harmonics generated in semiconductor nanostructures by the coupled dynamics of optical inter-and intraband excitations. *Physical Review B*, 77(7):075330, 2008.

[38] Emilio A Nanni, Wenqian R Huang, Kyung-Han Hong, Koustuban Ravi, Arya Fallahi, Gustavo Moriena, RJ Dwayne Miller, and Franz X Kärtner. Terahertz-driven linear electron acceleration. *Nature communications*, 6, 2015.

[39] LV Keldysh et al. Ionization in the field of a strong electromagnetic wave. *Sov. Phys. JETP*, 20(5):1307–1314, 1965.

[40] Michele Goano, Francesco Bertazzi, Michele Penna, and Enrico Bellotti. Electronic structure of wurtzite ZnO: Nonlocal pseudopotential and ab initio calculations. *Journal of Applied Physics*, 102(8):083709, 2007.

[41] Daniel Golde, Mackillo Kira, Torsten Meier, and Stephan W Koch. Microscopic theory of the extremely nonlinear terahertz response of semiconductors. *physica status solidi (b)*, 248(4):863–866, 2011.

[42] M. Abramowitz and I.A. Stegun. *Handbook of Mathematical Functions: with Formulas, Graphs, and Mathematical Tables*. Dover Books on Mathematics. Dover Publications, 2012.

[43] D. Kincaid and Ward Cheney. *Numerical Analysis: Mathematics of Scientific Computing*. Brooks/Cole, 3rd edition, 2002.

[44] Giulio Vampa, Chris McDonald, Alec Fraser, and Thomas Brabec. High-harmonic generation in solids: bridging the gap between attosecond science and condensed matter physics. *Selected Topics in Quantum Electronics, IEEE Journal of*, 21(5):1–10, 2015.